

Zero-Degree Auger Electron Spectroscopy of Projectile Ions

Theo J.M. Zouros* and Do-Hyung Lee†

The technique of zero-degree Auger projectile spectroscopy (ZAPS) is reviewed with particular emphasis on *high resolution* studies in energetic ion-atom collisions. The basic kinematic principles are discussed, aspects of the experimental apparatus including spectrometer and target cell are described in detail and selected topics of data analysis such as absolute normalization of cross sections to the Binary Encounter peak, and cross section determination of long-lived states are treated. Practical applications such as the precise determination of the projectile energy and the metastable beam fraction are also described. Finally, illustrations are presented from the use of this technique to explore basic collision mechanisms in double-capture, resonant transfer-excitation, electron-electron excitation and ionization, meV Coster-Kronig production and autodetachment of negative ions.

13.1 INTRODUCTION

In the past two decades considerable attention has been paid to the study of ion-atom collisions using highly charged ion projectiles. By limiting the number of electrons on the projectile and by using simple targets such as He or H₂, considerable simplification of the collision system is attained. Thus, the study of such fundamental atomic collision processes as excitation, ionization and capture, becomes considerably more tractable from both the experimental and the theoretical points of view. More recently, interest has focused on high

*) Department of Physics, University of Crete P.O. Box 2208, 71003 Heraklion and Institute of Electronic Structure and Laser, P.O. Box 1527, 71110 Heraklion, Crete, GREECE.
e-mail:tzouros@physics.ucl.ac.uk

†) Tennessee, Knoxville, TN 37996 and Oak Ridge National Laboratory, Physics Division, Bldg. 5500, MS-6377, Oak Ridge, TN 37831, USA.
e-mail:dhlee@utkux.utk.edu

resolution studies of projectile ions, which can provide state-selective information with important practical bearing on controlled thermonuclear fusion, astrophysics, and the possible creation of vuv and x-ray lasers [1,2]. Existing theories that have successfully predicted total cross-sections for these processes can now be tested to the next order of sophistication and accuracy by comparing with *state-selective differential* cross section measurements. Furthermore, few-electron systems are expected to provide one of the simplest testing grounds for studying the many-particle problem at large, and in particular, the role played by electron-electron interactions. [3–11]

In general, the lighter the projectile, the fewer the important channels available for ionization, capture or excitation of the projectile. Light projectiles have small fluorescence yields but much larger Auger electron yields, making the use of Auger spectroscopy particularly attractive for investigating low-Z projectile autoionizing states formed in the collision.

Projectile electron spectroscopy has been utilized for many years [12,13], since it enjoys a basic advantage over target electron spectroscopy, in that a large variety of highly charged ions have become increasingly available at collision energies and charge states readily controllable by the experimenter. However, kinematic line broadening effects [14,15], which become particularly large at high collision energies, have limited the usefulness of this technique, to rather low resolution ($> 1\%$) investigations [13]. These broadening effects were somewhat reduced at forward or backward observation angles [16] and studies of He- and Li-like projectile states at intermediate collision energies (~ 50 keV/u) were reported [17,18] at an observation angle of 6.4° . However, substantial reduction of kinematic broadening can be achieved at an observation angle of 0° or 180° with respect to the beam direction. This entails special instrumental provisions at these angles since the beam would have to pass through the spectrometer entrance slit without obstruction and still maintain good resolution. Today, the prevailing method uses a tandem spectrometer in which two analyzers are joined together in series. The first analyser really acts as a deflector, since fairly large slits have to be used to allow for the unobstructed passage of the ion beam, with a further aperture on the back side for the beam to exit. The second analyser with much narrower slits provides the high energy resolution. Resolution is further improved by decelerating electrons prior to energy analysis. Typical 0° spectra are shown in Fig. 13.1.

The first tandem spectrometers reported measurements at 180° for low keV/u collisions [19–21] and at 0° for fast (1–5 MeV/u) [22,23] and intermediate (15–150 keV/u) [24–26] collision energies. It was soon clear that high resolution measurements of unprecedented resolution ($\sim 0.1\%$ or better) were indeed possible at these angles and could provide state-selective information about projectile ions for a great variety of different collision systems and processes. [22,23,27,26,28] Thus, for example, zero-degree studies of basic collision processes such as transfer-excitation [24,29], double electron capture

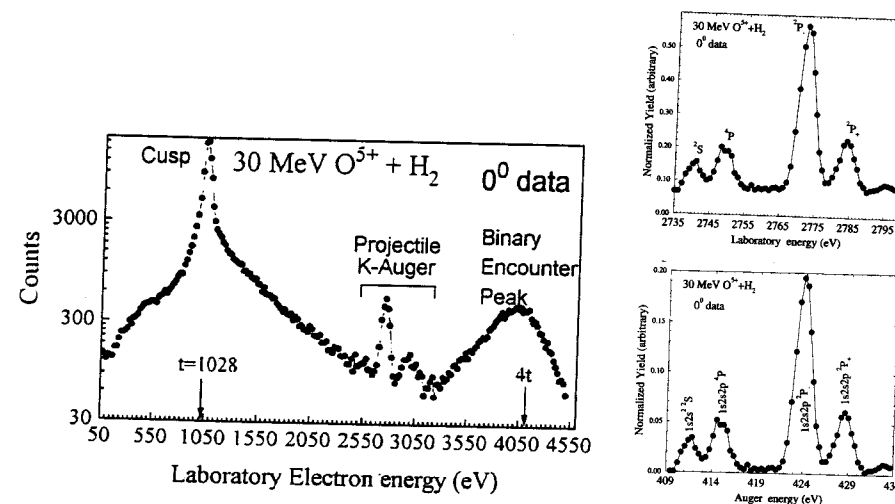


FIGURE 13.1 Typical electron spectra taken at 0° observation angle for 30 MeV O^{5+} collisions with H_2 using a tandem electron spectrometer. Left: The electron energy range from 50–4500 eV is displayed in low resolution showing the basic features of such a spectrum: (a) the Cusp peak at electron energy $t = \frac{1}{2}mV_p^2$, (b) the Oxygen (projectile) K-Auger peaks, (c) the Binary Encounter electron (BEE) peak centered near an energy of $4t$, resulting from target ionization. Right: High resolution spectrum of just the largest projectile K-Auger peak (left) obtained by decelerating the electrons prior to energy analysis to an energy $\epsilon_{pass} = 200$ eV. Four major lines are revealed that can be associated with excitation. Top: laboratory frame. Bottom: projectile rest frame after background subtraction.

[30–32,25,33,34], resonance-transfer excitation [35–39], e-e excitation [40–42] and e-e ionization [43,8] yielded new state-selective cross section information about collision mechanisms. Studies of atomic structure [44–47], Rydberg states produced in gases or foils [48,27,49,50], low energy Coster-Kronig transitions [51,52], autodetachment of negative ions [53–57], as well as a variety of other collision phenomena [58–62] involving high resolution spectroscopy of charged ions were also very successful. Zero-degree projectile electron spectroscopy studies have been particularly effective at electrostatic accelerators, where the collision energy can be changed easily, thus providing means to study the energy dependence of the collision mechanisms.

Today, the technique of zero-degree Auger projectile spectroscopy (ZAPS) is being used by an increasing number of accelerator facilities in the US, Europe, South America and Japan to investigate properties of highly charged ions at collision energies ranging from a few keV to hundreds of MeV. There have already been a number of reviews and progress reports [48,27,63,26,64–66,7,28,67,68] on high resolution and zero-degree Auger pro-

jectile spectroscopy. Here we limit our presentation to details of the technique that are not so well known. In particular, after briefly discussing some of the basic principles of zero-degree projectile electron spectroscopy, we take a more detailed look at various aspects of the experimental set-up. We go on to the determination of *absolute* differential cross sections for prompt and long-lived autoionizing states by normalizing to the Binary Encounter peak. Practical applications such as the determination of the projectile beam energy and the metastable beam fraction are also discussed. Finally, examples from the recent literature are provided, demonstrating both the methodology and the physics that can be studied by applying ZAPS to the investigation of few electron projectiles in collisions with H_2 and He targets.

13.2 PRINCIPLES OF PROJECTILE AUGER ELECTRON SPECTROSCOPY

The basic goal of ZAPS is to provide high resolution electron spectra from which both atomic structure and cross section information can be obtained. To date, ZAPS has been particularly effective in providing state-resolved K-Auger spectra for collisions of low- Z ions ($2 \leq Z \leq 10$) with H_2 and He. To obtain high quality spectra ZAPS takes advantage of the kinematic properties of electrons ejected from moving emitters, as well as the inner-shell vacancy production mechanism of "ion surgery" applicable in fast collisions with light targets. These two aspects are described next.

13.2.1 Kinematics of electrons from moving emitters

Kinematic effects can severely influence the shape, width and energy of the projectile Auger lines. The analysis of such effects [69,14,70,15,71,72,27] is in general complicated and model dependent since the projectile Auger electron is emitted from the *scattered* projectile. However, in energetic collisions of a few MeV/u or larger, of particular interest here, projectile ions are mostly scattered through very small angles (\sim mrads) with minimum energy loss and negligible effect on the trajectory of the emitted electrons. We may thus assume for simplicity that the projectile ion scattering angle is zero and use simple velocity vector addition, to directly determine the projectile-to-laboratory frame transformations, particularly in the case of zero-degree observation, where the best resolution is possible.

Using the velocity addition diagrams shown in Fig. 13.2, the electron kinetic energy $\varepsilon' = \frac{1}{2}mv'^2$ in the projectile rest frame is related to the corresponding laboratory kinetic energy $\varepsilon = \frac{1}{2}mv^2$ by:

$$\varepsilon' = \varepsilon + t - 2\sqrt{\varepsilon t} \cos \theta \quad (13.1a)$$

or equivalently,

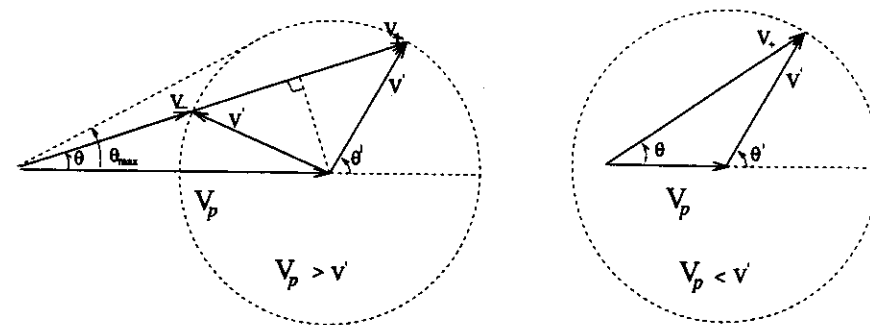


FIGURE 13.2 Projectile electron kinematics. The electron velocity in the laboratory frame $\mathbf{v} = \mathbf{V}_p + \mathbf{v}'$ where \mathbf{V}_p is the projectile velocity and \mathbf{v}' is the electron velocity in the projectile rest frame. The electron ejection angles are θ and θ' in the two frames, respectively. For $V_p > v'$ two solutions, v_{\pm} , are possible with $\theta \leq \theta_{max}$. Reprinted from "High resolution studies of two-electron processes observed in energetic ion-atom collisions via zero-degree Auger spectroscopy", T. J. M. Zouros, D. Schneider, and N. Stolterfoht, *Nuc. Instr. Meth. B31* (1988) 349, with kind permission from Elsevier Science - NL, Sara Burgerhartstraat 25, 1055 KV Amsterdam, The Netherlands.

$$\varepsilon = \varepsilon' + t + 2\sqrt{\varepsilon' t} \cos \theta' \quad (13.1b)$$

where θ and θ' are the ejection angles of the electron in the laboratory and projectile rest frame, respectively. The quantity t is equal to the energy of an electron moving with the velocity of the projectile, $t = \frac{1}{2}mV_p^2 = \frac{m}{M_p}E_p$, where E_p and M_p are the projectile energy and mass, respectively. It is convenient to introduce the universal dimensionless parameter:

$$\zeta \equiv \sqrt{\frac{t}{\varepsilon'}} \quad (13.2)$$

For fast emitters ($V_p > v'$ or equivalently $\zeta > 1$), as shown in Fig. 13.2, there can be two possible solutions (\pm) obtained by solving Eq 13.1a for ε as a function of θ :

$$\varepsilon_{\pm}(\theta) = \varepsilon' (\zeta \cos \theta \pm \sqrt{1 - \zeta^2 \sin^2 \theta})^2 \quad (\zeta > 1, 0 \leq \theta \leq \theta_{max} = \sin^{-1} \frac{1}{\zeta}) \quad (13.3a)$$

$$\varepsilon(\theta) = \varepsilon' (\zeta \cos \theta + \sqrt{1 - \zeta^2 \sin^2 \theta})^2 \quad (\zeta \leq 1, 0^\circ \leq \theta \leq 180^\circ) \quad (13.3b)$$

Clearly, $\zeta^2 \sin^2 \theta \leq 1$, results in a lower limit on the electron energies accessible to our spectrometer. However, for $\theta = 0^\circ$, the whole energy range is accessible and we have from Eq. 13.3:

$$\varepsilon_+ = (\sqrt{\varepsilon'} + \sqrt{t})^2 = \varepsilon' (1 + \zeta)^2 \quad (\text{all } \zeta, \theta = 0^\circ) \quad (13.4a)$$

$$\varepsilon_- = (\sqrt{\varepsilon'} - \sqrt{t})^2 = \varepsilon' (1 - \zeta)^2 \quad (\zeta > 1, \theta = 0^\circ) \quad (13.4b)$$

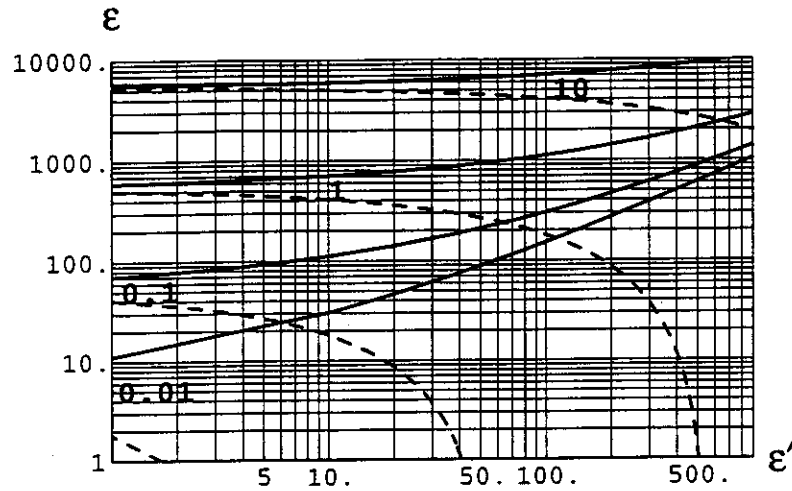


FIGURE 13.3 Relation between rest frame energies ε' (eV) and the laboratory frame ε (eV) at $\theta = 0^\circ$ for $E_p = 0.01, 0.1, 1, 10$ MeV/u. Continuous lines correspond to the (+) solutions, while dashed lines to the (-) solutions of Eq. 13.4.

where the (+) sign refers to the higher and the (-) sign to the lower laboratory electron energy corresponding to rest frame ejection angles $\theta' = 0^\circ$ or 180° , respectively, in the case of fast emitters. Thus, a doubling of the Auger line is observed in the laboratory frame [27]. In Fig. 13.3 the relation between the rest frame energies ε' and the laboratory frame energy ε is given for four different collision energies and $\theta = 0^\circ$.

Kinematic effects arising from the above relations affecting the detected electron yields and line shapes are discussed next.

Line broadening

Clearly, as indicated in Eqs. 13.1, both the finite acceptance angle $\Delta\theta$ and the uncertainty in the projectile energy, Δt , can give rise to an uncertainty $\Delta\varepsilon$ in the detected laboratory electron energy ε , independent of the specific energy resolution of the spectrometer utilized. This inherent energy uncertainty results in the overall broadening of the Auger lines.

In general, for non-zero ($\theta \neq 0^\circ$) observation angles the dominant effect arises from the finiteness of $\Delta\theta$. However, this so called kinematic line broadening, ΔB_θ , is much reduced when electron observations are performed at $\theta = 0^\circ$. In this case, and depending on the energy resolution of the accelerator utilized, the line broadening ΔB_t arising from the finite uncertainty Δt , can

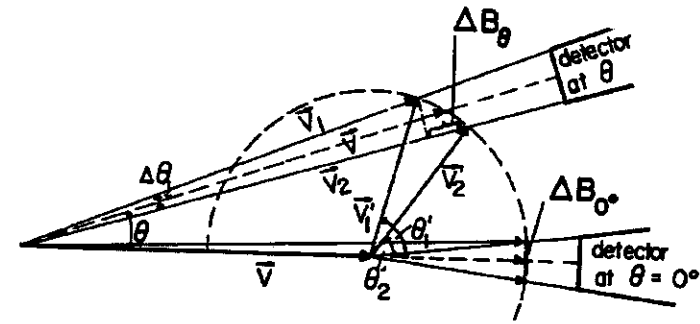


FIGURE 13.4 Geometric demonstration of kinematic line broadening for spectrometer with acceptance angle $\Delta\theta$ placed at the laboratory observation angle θ . Two electrons having identical speeds $v'_1 = v'_2$ in the projectile frame but ejected at different angles θ'_1 and θ'_2 will be detected in the lab within $\Delta\theta$ with different speeds $v_1 \neq v_2$, resulting in a kinematic energy broadening, $\Delta B_\theta \sim |\frac{1}{2}mv_1^2 - \frac{1}{2}mv_2^2|$. At $\theta = 0^\circ$ (or 180°), ΔB_θ is minimized.

become as significant as ΔB_{0° . In the next two sections we discuss these two broadening effects in more detail.

a. Kinematic line broadening

Electrons detected at non-zero laboratory angles ($\theta \neq 0^\circ$), as demonstrated in Fig. 13.4, can originate from a range of different angles θ' in the projectile rest frame due to the finite acceptance angle $\Delta\theta$ of the electron spectrometer. Thus, two electrons having the *same* energy ε' and *different* ejection angles θ'_1 and θ'_2 , in the projectile rest frame, detected within an acceptance angle $\Delta\theta$, will correspond to *different* laboratory velocities \vec{v}_1 and \vec{v}_2 with corresponding energies $\varepsilon_1 \neq \varepsilon_2$, as indicated in Fig. 13.4. A net energy broadening ΔB_θ results, with $\Delta B_\theta \sim |\varepsilon_1 - \varepsilon_2|$. However, at $\theta = 0^\circ$ and 180° , as seen by a careful inspection of Fig. 13.4, ΔB_θ is substantially reduced. Furthermore, it is clear that ΔB_θ increases with collision energy.

The kinematic broadening may be computed exactly:

$$\Delta B_\theta^{\text{exact}} = \begin{cases} |\varepsilon(\theta + \Delta\theta/2) - \varepsilon(\theta - \Delta\theta/2)| & \text{for } \theta \in (\frac{\Delta\theta}{2}, \pi - \frac{\Delta\theta}{2}) \\ |\varepsilon(\theta + \Delta\theta/2) - \varepsilon(0^\circ)| & \text{for } \theta \in [0, \frac{\Delta\theta}{2}] \text{ or } [\pi - \frac{\Delta\theta}{2}, \pi] \end{cases} \quad (13.5)$$

Further insight can be gained by expanding $\Delta B_\theta^{\text{exact}}$ in a Taylor series in powers of $\Delta\theta$:

$$\Delta B_{\theta}^{exact} \approx \left| \sum_n \frac{\partial^n \varepsilon(\theta)}{\partial \theta^n} \frac{(\Delta \theta)^n}{n!} \right| = \left| \sum_n \Delta B_{\theta}^{(n)} \right| \quad (13.6)$$

By differentiating Eq. 13.1a with respect to θ and using Eq. 13.3, the expansion coefficients can be obtained in terms of ε' and θ . Thus, to first order in $\Delta \theta$ we have:

$$\Delta B_{\theta}^{(1)} = -2\Delta \theta \sin \theta \frac{\sqrt{\varepsilon t}}{1 - \sqrt{\frac{t}{\varepsilon}} \cos \theta} \quad (13.7a)$$

$$= \mp 2\Delta \theta \sin \theta \varepsilon' \zeta \frac{(\zeta \cos \theta \pm \sqrt{1 - \zeta^2 \sin^2 \theta})^2}{\sqrt{1 - \zeta^2 \sin^2 \theta}} \quad (13.7b)$$

which is seen to depend on $\sin \theta$ and therefore $\Delta B_{\theta}^{(1)} = 0$ at $\theta = 0^\circ$ or 180° . For $\theta = 0^\circ$ or 180° we thus need to calculate the second order broadening contribution $\Delta B^{(2)}$, which is now dominant. For $\theta = 0^\circ$ (remembering to set the effective angular range to $\Delta \theta/2$), we use the above procedure to obtain: [27]

$$\Delta B_{0^\circ}^{(2)} = \left(\frac{\Delta \theta}{2}\right)^2 \frac{\varepsilon}{|1 - \sqrt{\frac{\varepsilon}{t}}|} \quad (13.8a)$$

$$= \left(\frac{\Delta \theta}{2}\right)^2 \varepsilon' \zeta (1 \pm \zeta)^2 \quad (13.8b)$$

Typical values of $\Delta B_{0^\circ}^{(2)} \sim 0.5 - 10$ eV for Auger energies $\varepsilon' \sim 100 - 1000$ eV and collision energies, $E_p \sim 1 - 10$ MeV/u. A rough estimate for $5^\circ < \theta < 170^\circ$ shows that $\Delta B_{0^\circ}^{(2)}/\Delta B_{\theta}^{(1)} \sim \Delta \theta$. For typical detector acceptance angles $\sim 1^\circ$ ($\Delta \theta \sim 0.02$ radians), $\Delta B_{0^\circ}^{(2)} \sim 100 - 400$ times smaller than $\Delta B_{\theta}^{(1)}$. Thus, substantial reduction of the kinematic broadening occurs at $\theta = 0^\circ$ where the first-order term vanishes. In Fig. 13.5 (top), the ratio of $R = \Delta B_{\theta}^{exact}/\Delta B_{0^\circ}^{exact}$, is plotted as a function of ζ and θ . The inaccessible region marked by the white space results from the limitation $\theta \leq \theta_{max}$ of Eq. 13.3a. Large values of R indicate regions of large kinematic broadening. A ridge of maximum broadening is observed around $\theta = 50^\circ$ which spreads to larger angles for decreasing values of ζ . It is reminded that cylindrical mirror analyzers are normally used at 42.3° in target spectroscopy. [13] Clearly this would be a bad choice for high resolution projectile electron spectroscopy. At backward angles near $\theta \sim 180^\circ$, a region of relatively low kinematic broadening is seen to exist, as indicated in Fig. 13.5 (top), which remains largely unexplored by high resolution projectile spectroscopy.

Computing the relative broadening, $R_{\Delta B_{\theta}^{(2)}}$, we obtain the simple result: [73]

$$R_{\Delta B_{\theta}^{(2)}} \equiv \frac{\Delta B_{\theta}^{(2)}}{\varepsilon} = \left(\frac{\Delta \theta}{2}\right)^2 \zeta \quad (\theta = 0^\circ \text{ or } 180^\circ) \quad (13.9)$$

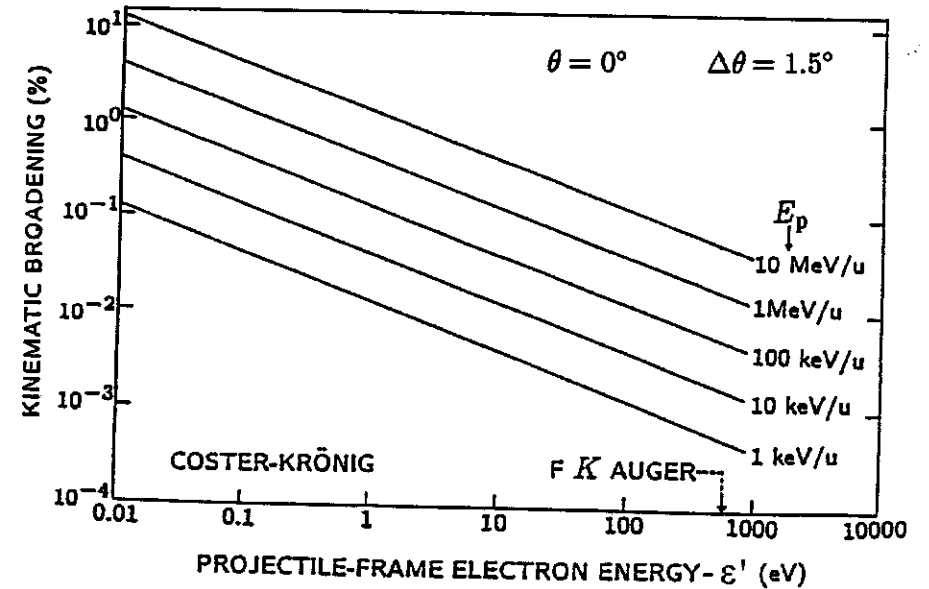
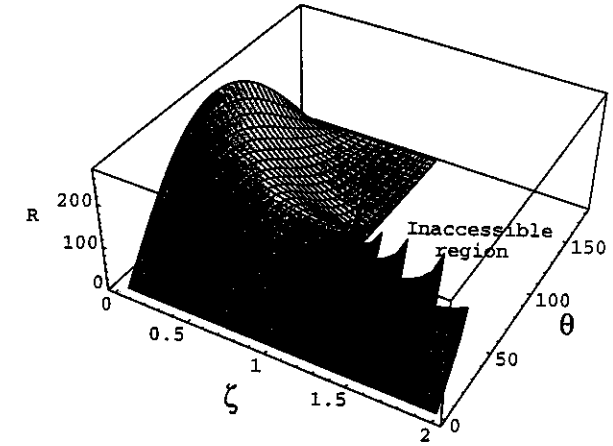


FIGURE 13.5 Top: $R = \Delta B_{\theta}^{exact}/\Delta B_{0^\circ}^{exact}$ (see Eq. 13.5) plotted as a function of $\zeta = \sqrt{t/\varepsilon'}$ and θ (degrees) for an acceptance angle $\Delta \theta = 1.5^\circ$. Bottom: Relative kinematic broadening, $\Delta B_{0^\circ}^{(2)}/\varepsilon$ (see Eq. 13.9) plotted as a function of Auger energy for different projectile energies E_p (adapted from Ref. [73]).

$R_{\Delta B_0^{(2)}}$ is plotted in Fig. 13.5 as a function of the Auger energy ε' for a few characteristic values of the projectile energy. Clearly, ZAPS applications where Auger energies are large and the collision slow, such as in heavier-Z projectiles increasingly available at storage rings, EBIS and ECR sources [30–32,25,33,34] can be expected to have the best resolution.

It is interesting to compute $\Delta B_\theta^{(2)}$ for $\theta = 180^\circ$. The accessible energy range is now limited though, since $\zeta < 1$. The following relations hold:

$$\varepsilon = (\sqrt{\varepsilon'} - \sqrt{t})^2 \quad (\zeta \leq 1, \theta = 180^\circ) \quad (13.10a)$$

$$\Delta B_{180^\circ}^{(2)} = \left(\frac{\Delta\theta}{2}\right)^2 \frac{\varepsilon}{1 + \sqrt{\frac{\varepsilon}{t}}} \quad (13.10b)$$

$$= \left(\frac{\Delta\theta}{2}\right)^2 \varepsilon' \zeta (1 - \zeta)^2 \quad (13.10c)$$

Comparing the 2nd order broadenings at $\theta = 0^\circ$ and 180° for $\zeta < 1$ we have:

$$\frac{\Delta B_{180^\circ}^{(2)}}{\Delta B_{0^\circ}^{(2)}} = \left(\frac{1 - \zeta}{1 + \zeta}\right)^2 \quad (13.11)$$

indicating that $\Delta B_{180^\circ}^{(2)}$ is always smaller than $\Delta B_{0^\circ}^{(2)}$. Furthermore, since electrons are kinematically shifted to lower energies at this observation angle, smaller deceleration factors can be used entailing smaller losses in transmission. Thus, in principle, good quality measurements should be possible at 180° , with even higher resolution than at 0° . A clear drawback is the energy limitation of $\zeta < 1$ (part of the inaccessible region of Fig. 13.5) making this method impractical for fast collisions ($t > 1000$ eV) unless higher-Z projectiles with larger Auger energies are studied. The few measurements reported at 180° , to date, have indeed been performed at very low collision energies (few keV/u) with good results [19–21].

b. Line broadening due to energy spread of the emitter

The emitter energy-spread broadening ΔB_t due to the variation in t , the reduced projectile energy, can be computed to first order from $\Delta B_t^{(1)} = \Delta t \partial \varepsilon / \partial t$ [27], using Eq. 13.1a. For $\theta = 0^\circ$ observation we obtain:

$$\Delta B_t^{(1)} = \left(\frac{\Delta t}{t}\right) \varepsilon' \zeta |1 \pm \zeta| \quad (\theta = 0^\circ) \quad (13.12)$$

Comparing this to the 2nd order kinematic broadening $\Delta B_{0^\circ}^{(2)}$ given by Eq. 13.8b we obtain:

$$\frac{\Delta B_t^{(1)}}{\Delta B_{0^\circ}^{(2)}} = \frac{\left(\frac{\Delta t}{t}\right)}{\left(\frac{\Delta\theta}{2}\right)^2} \frac{1}{(\zeta \pm 1)} \quad (\theta = 0^\circ) \quad (13.13)$$

TABLE 13.1 Calculated line broadenings for 5–33 MeV collisions of F^{6+} ions. Corresponding spectra appear in Fig. 13.25 (left). The K-State zero-degree tandem spectrometer parameters given in Table 13.2 have been used in this calculation together with a beam energy spread $\Delta t/t = 7 \times 10^{-4}$, Auger energy $\varepsilon'_A = 567.8$ eV and width $\Gamma' = 80.5$ meV where $\Gamma = |1 + \zeta| \Gamma'$ (see Eq. 13.16). The pass energy ε_{pass} used and the instrumental energy width $\Delta \varepsilon_{ins} = R_{ins} \varepsilon_{pass}$ are also listed. The limiting acceptance angle, $\Delta \theta_{lim}$ (see Eq. 13.15) is seen to be almost double the spectrometer acceptance angle $\Delta \theta = 1.17^\circ$ suggesting that better optimization of spectrometer parameters is possible for the study of this particular Auger line. The computed limiting pass energy ε_{pass}^{lim} (see Eq. 13.19) indicates that resolution can also in principle be improved.

E_p (MeV)	t (eV)	ζ $\sqrt{\frac{t}{\varepsilon'_A}}$	ε_+ (eV)	$\Delta B_{0^\circ}^{(2)}$ (meV)	$\Delta B_t^{(1)}$ (meV)	Γ (meV)	Γ_{tot} (meV)	$\Delta \varepsilon_{ins}$ (meV)	ε_{pass} (eV)	$\Delta \theta_{lim}$ (°)	ε_{pass}^{lim} (eV)
4.75	137	0.492	1263	64.6	291	119	191	2756	100	2.5	7
14.25	411	0.851	1946	172	626	147	357	5513	200	2.2	13
16.63	480	0.919	2092	200	701	153	395	4135	150	2.2	14
19	549	0.983	2233	228	775	158	434	5513	200	2.2	16
26.125	754	1.153	2631	315	986	171	545	5513	200	2.1	20
33.25	960	1.300	3004	406	1189	183	654	5513	200	2.0	24

For tandem accelerators, $\Delta t/t \sim 3 - 9 (\times 10^{-4})$ and is seen to be of the same order as $(\Delta\theta)^2$ for $\Delta\theta \sim 1^\circ - 1.5^\circ$. Hence, ΔB_t may be larger than $\Delta B_{0^\circ}^{(2)}$ for typical ZAPS applications ($\zeta = 1.1 - 2$ for the (+) solution). In Table 13.1 an example of the calculated broadenings is shown.

We can combine the two broadenings and the stretched natural line width Γ (see Eq. 13.16 below) in quadrature [27] to obtain an estimate of the total laboratory line width (FWHM), Γ_{tot} :

$$\Gamma_{tot} = \sqrt{(\Delta B_t/2)^2 + (\Delta B_{0^\circ}/2)^2 + \Gamma^2} \approx \sqrt{(\Delta B_t^{(1)}/2)^2 + (\Delta B_{0^\circ}^{(2)}/2)^2 + \Gamma^2} \quad (13.14)$$

assuming ΔB_t and ΔB_{0° to relate to the base width of the Auger line profile. We note that a general analysis should also include effects due to azimuthal broadening, the variation in the projectile scattering angle and other effects which have been ignored in this analysis since they are usually small in ZAPS applications. More details can be found in Refs. [69,14,70,15,71,72,27] and references therein.

Clearly to obtain experimental resolutions of the order of the natural line width Γ the sum of the main broadenings considered here has to be minimized. The experimental resolution and the kinematic broadening, can be decreased, within limits, by decreasing the dimensions of the analyser apertures, increasing the spectrometer size and/or decreasing the pass energy ε_{pass} . However,

as mentioned above, the usual limiting factor is the beam energy spread. On tandem accelerators terminal ripple (typically a few kV per charge state), affects the highest projectile charge states the most. For example, a 35 MeV F^{8+} beam at the K-State tandem has a typical $\Delta t/t \sim 7 \times 10^{-4}$. LINACs using time bunching will be affected even more, typical values being about double those for tandems. Storage rings using electron cooling have smaller values, with $\Delta t/t \sim 0.3 - 1.5 \times 10^{-4}$ depending on beam current and energy. On these machines, effective beam currents are large ($\sim \mu A$), making them particularly attractive for high resolution measurements. To date ZAPS has not been used with stored ions.

Clearly, if $\Delta B_{0^{\circ}}^{(2)} \sim \Delta B_t^{(1)}$ both broadenings must be reduced simultaneously if better resolution measurements are to be possible. Thus, setting $\Delta B_{0^{\circ}}^{(2)} = \Delta B_t^{(1)}$ a useful lower limit for the spectrometer acceptance angle may be established:

$$\Delta\theta \geq \Delta\theta_{lim} \equiv \frac{2}{|1 \pm \zeta|} \sqrt{\frac{\Delta t}{t}} \quad (13.15)$$

Line shifting

The Auger line energy ϵ' is shifted by the additional two terms on the right hand side of Eq. 13.1b to a higher energy ϵ in the lab frame. For fast projectiles ($\zeta \gg 1$) the shift follows primarily from the second term, t . Furthermore, for $\zeta \gg 1$, as already discussed, Auger lines can only be observed within a narrow range of forward angles.

The effect of line shifting may be favorably applied to measurements where the Auger energy ϵ' is very small. By kinematically shifting the Auger lines to higher energies, basic instrumental problems such as contact potentials or inadequate shielding of the earth's magnetic field may be overcome with little effort. In fact, using this technique, electrons from the Auger decay of high Rydberg states [48,27,51,52] or shape-resonances of negative ions [53–57] formed in ion-atom collisions have been measured with high resolution. Measurements of autoionization energies in the meV range, otherwise impossible to access, have been reported. In Fig. 13.6, spectra with two autoionizing lines [28,52] having rest energies of 60 meV and 100 meV are shown. Other examples are shown in Fig. 13.27 when discussing studies of negative ions.

For very fast projectiles the electron energies of the (+) solution can become too large for the typical spectrometer range (maximum energies $\sim 5 - 6$ keV). In this case, the lower energy solution (–) may be used [27].

Line stretching

The width of the Auger lines is changed according to the third term on the right hand side of Eq. 13.1b. For zero-degree measurements, we have: [27]

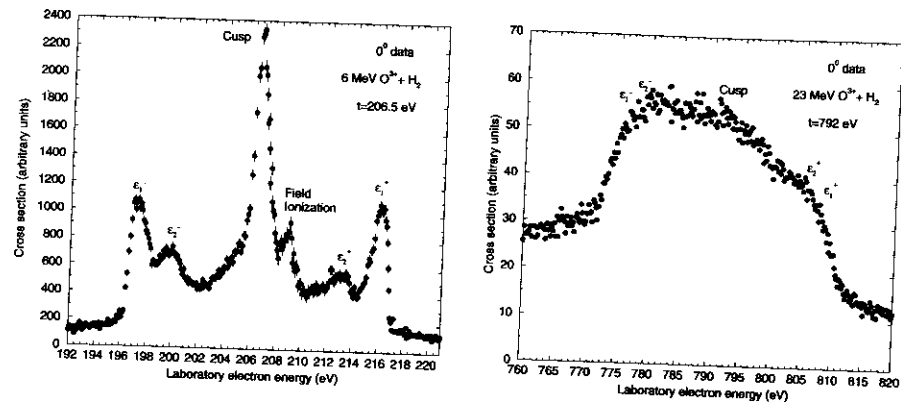


FIGURE 13.6 Zero-degree observation of meV electrons from autoionizing states produced by excitation in O^{3+} collision with H_2 . [52,74] The two lines at $\epsilon_{1,2}^{\pm}$ on either side of the Cusp have rest frame energies $\epsilon_1' \sim 100$ meV and $\epsilon_2' \sim 60$ meV, respectively. For both spectra $\epsilon_{pass} = 10$ eV giving an instrumental resolution $\Delta\epsilon_{ins} = 280$ meV. Left: 6 MeV collisions, $\Delta B_{0^{\circ}}^{(2)} \sim 1.01$ eV with $\Delta\theta = 1.17^{\circ}$ and $\Delta B_t^{(1)} \sim 0.3$ eV. The small peak just to the right of the Cusp is due to field ionization of projectile Rydberg electrons [75–77] inside the first stage of the tandem spectrometer. Right: Same spectrum but for 23 MeV collisions, $\Delta B_{0^{\circ}}^{(2)} \sim 7.45$ eV and $\Delta B_t^{(1)} \sim 1.1$ eV. Here the kinematic broadening, which increases with projectile velocity, completely washes out the peak structure. Other reasons for the strange looking spectrum are under investigation. A beam energy spread of $\frac{\Delta t}{t} = 7 \times 10^{-4}$ was assumed in the calculation of $\Delta B_t^{(1)}$.

$$\Delta\epsilon = |1 \pm \zeta| \Delta\epsilon' \quad (\theta = 0^{\circ}) \quad (13.16)$$

resulting in stretching of the line shape for the (+) solution and compression for the (–) solution. The effect of line stretching may be favorably applied to measurements requiring extremely high resolution, such as the measurements of natural line widths. Light atoms have Auger line widths $\Gamma_a^v \sim 0.1$ eV. Hence, it is useful to stretch the line kinematically so that its width becomes comparable to the spectrometer resolution. In Fig. 13.7 Auger lines resulting from intermediate energy $He^+ + He$ collisions [24,27] are shown in the lab frame and also after transformation to the projectile frame.

The 3P line width is seen to be 0.10 eV in the projectile rest frame. Since this line is known to have a much narrower natural line width (0.010 eV see Ref. [78]) the measured width is clearly due to the much larger instrumental resolution. The stretching factor $(1 + \zeta)$ is 2.3 and helps appreciably to determine the natural width of the 1S line which amounts to 0.14 eV and 0.32 eV in the projectile and laboratory frames, respectively, after the instrumental resolution has been unfolded.

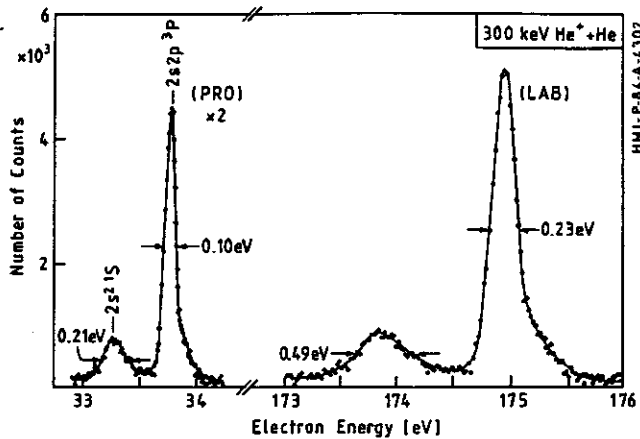


FIGURE 13.7 Kinematic line stretching and enhancement. Projectile autoionization lines (right) in 300 keV collisions of ${}^3\text{He}^+ + \text{He}$ are kinematically stretched-out and enhanced when observed in the laboratory frame (LAB). The same spectrum transformed to the projectile rest frame (PRO) is shown on the left. Note the factor of 2 used to multiply the rest frame electron yield. This spectrum was obtained by decelerating electrons to a pass energy, $\varepsilon_{\text{pass}} = 7$ eV. The spectrometer had an acceptance angle $\Delta\theta \sim 2.1^\circ$ giving a kinematic broadening of $\Delta B_0^{(2)} = 0.076$ eV. Reprinted from “High resolution studies of two-electron processes observed in energetic ion-atom collisions via zero-degree Auger spectroscopy”, T. J. M. Zouros, D. Schneider, and N. Stolterfoht, *Nuc. Instr. Meth. B31* (1988) 349, with kind permission from Elsevier Science - NL, Sara Burgerhartstraat 25, 1055 KV Amsterdam, The Netherlands.

It should be emphasized that stretching and broadening refer to qualitatively different effects. The first one originates from the transformation properties implied in Eqs. 13.1, while the second arises primarily due to the finite acceptance angle of the electron spectrometer, as shown in Eq. 13.8. Accordingly, the stretching effect leaves intrinsic structures of the Auger spectrum unchanged, whereas the broadening effect tends to wash them out.

Line enhancement

Another consequence of projectile-electron kinematics is that the laboratory electron yield is enhanced with respect to the rest frame yield by the stretching factor. This was already evident in the example of Fig. 13.7. The frame transformation for the double differential cross sections is given by: [27]

$$\frac{d^2\sigma}{d\varepsilon d\Omega} = |1 \pm \zeta| \frac{d^2\sigma}{d\varepsilon' d\Omega'} \quad (\theta = 0^\circ) \quad (13.17)$$

resulting in enhancement of the laboratory lines for the (+) solution and diminishment for the (-) solution.

Angular compression

The well known “beaming” effect observed for X rays emitted from relativistic emitters, is also observed for electrons ejected from fast projectile ions. Electrons emitted *isotropically* in the rest frame will be ejected into a narrow beam in the forward direction in the laboratory frame. The transformation of the angular range can be calculated from the angle transformation obtained directly from Fig. 13.2:

$$\sin \theta = \sqrt{\frac{\varepsilon'}{\varepsilon}} \sin \theta' = \frac{\sin \theta'}{\sqrt{1 + 2\zeta \cos \theta' + \zeta^2}} \quad (13.18)$$

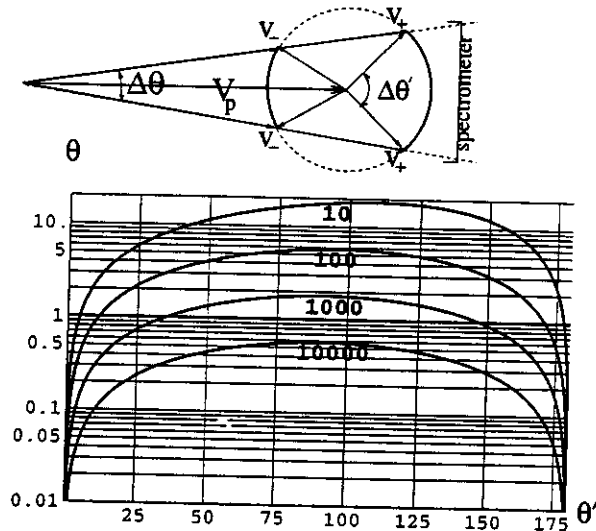


FIGURE 13.8 Angular compression in very fast emitters. Top: The angular range $\Delta\theta'$ in the forward and backward directions in the projectile rest frame (thick dark arcs) is compressed into the spectrometer acceptance angle $\Delta\theta$. Bottom: Relation between θ (degrees) and θ' (degrees) for $\zeta^2 : 10, 10^2, 10^3, 10^4$ (see Eq. 13.18). For $\zeta^2 = 10^4$, the whole rest frame angular range $\theta' = 0^\circ - 180^\circ$ is seen to be compressed into the laboratory range of $\theta = 0^\circ - 0.6^\circ$ completely covered by the typical spectrometer acceptance angle $\Delta\theta \sim 1.2^\circ$. The range $0^\circ \leq \theta' \leq 90^\circ$ gives rise to the (+) solutions, while the range $90^\circ \leq \theta' \leq 180^\circ$ gives rise to the (-) solutions.

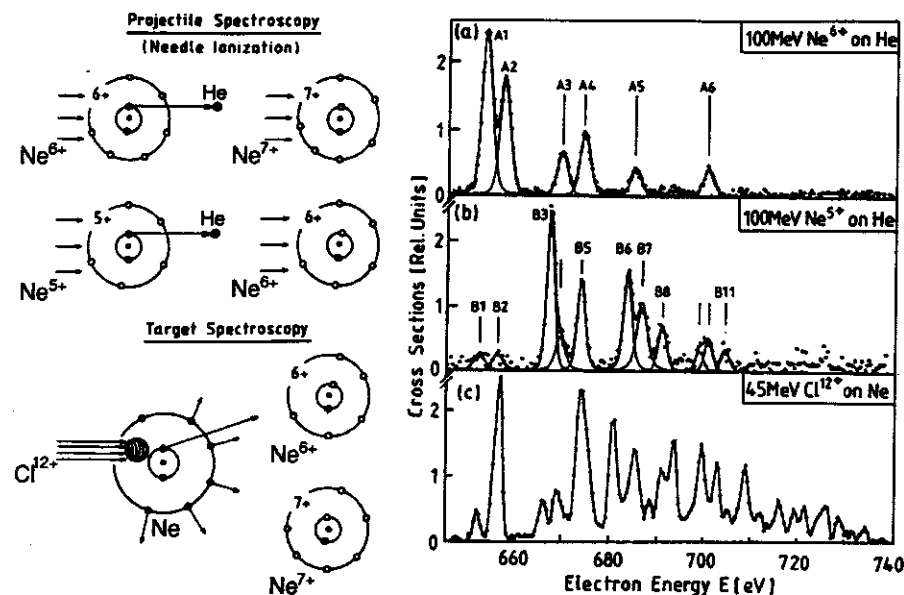


FIGURE 13.9 Demonstration of needle ionization: When a projectile collides with light target atoms, an inner vacancy is produced while its outer-shell structure is preserved with only a single final projectile charge-state emerging. Simple spectra result, as shown in the Ne K-Auger spectra on the right. The observed Auger lines in (a)-(b) are characteristic of Li- and Be-like ions resulting from the removal of a single $1s$ electron from the impinging configuration. In the opposite situation (c), encountered from an example in target spectroscopy, a *heavy* projectile collides with a heavy target, resulting in many different target states which give rise to complicated Auger spectra [79] with severe line blending (figures adapted from Ref. [27]).

For large values of ζ^2 this can result in severe compression of the rest frame angular distribution as demonstrated in Fig. 13.8. In such cases, e.g. for $\zeta \sim 10^2$, angular information will be washed out due to the resulting averaging over the large angular range in the rest frame [52]. Thus, angular compression and kinematic broadening are seen to be closely linked. In the example shown in Fig. 13.6, for 6 MeV O^{3+} collisions, $\zeta^2 \sim 2000$ and thus the rest frame range $|\theta'| \leq 22^\circ$ gets compressed into the acceptance angle $\Delta\theta = 1^\circ$ of the spectrometer at $\theta = 0^\circ$. For 23 MeV collisions beaming is more extreme with $|\theta'| \leq 50^\circ$ compressed into $\Delta\theta = 1^\circ$.

We finally note that when $\varepsilon < \varepsilon'$, as for example in the case of backward observation angles for slow emitters (see Eq. 13.3b), Eq. 13.18 shows that an angular expansion occurs instead of compression.

13.2.2 Ion surgery

It is well known from target spectroscopy that light projectiles such as photons, electrons or protons have the ability to selectively excite or ionize a single $1s$ target electron without disturbing the outer-shell electrons [80,81]. This effect has also been used advantageously in high resolution *projectile* K-x-ray spectroscopy, [82–85] using light targets such as H_2 or He. The situation is shown schematically in Fig. 13.9 (left) and has been referred to as “ion surgery” [63] and in the case of ionization (excitation) as “needle” ionization (excitation) [22,23].

Ion surgery conditions prevail in fast collisions [44,63], where the probability for electron capture and double-excitation processes is small. Then projectile K-Auger lines result predominantly from the $1s \rightarrow nl$ excitation or $1s$ ionization of the incoming ion. The line identification is greatly facilitated due to the simple structure of the spectra as shown in the example of Fig. 13.9 (right) (a)-(b). Much more complicated spectra can arise in the opposite situation, shown in Fig. 13.9 (c), where many different target charge states are produced resulting in severe line blending [79]. These target spectra result from the ionization of a target by a *heavy* projectile. Ion surgery has played an important role in almost all ZAPS measurements to date. It is specifically invoked in section 13.5.1 and used in the determination of the fraction of metastable ions in a beam of Be-like ions.

13.3 EXPERIMENTAL SET-UP

Both target and projectile electron spectroscopy use very similar apparatus. Thus, the beam line, scattering chamber, electronics and data acquisition are common in both cases. Here we shall only present details that are particular to ZAPS.

The experimental set-up for ZAPS used at the HMI-Berlin [22] is shown in Fig. 13.10. Most other setups have been modeled after this one. In Fig. 13.11 the KSU setup is shown [76].

13.3.1 Gas target

A differentially pumped target cell is used to give a well defined interaction length. Excitation and decay of the projectile takes place primarily within this cell. The gas cell should be operated at pressures sufficiently low for single collision conditions to prevail for *every* observed line of interest [25]. Typical gas cells used are about 5–10 cm long and run at pressures of a few mTorr. A capacitive manometer can be used for accurate absolute pressure readings. Differential pumping of the cell is usually performed by the main chamber pump. The chamber pressure with gas cell running should be better than $1 - 2 \times 10^{-5}$ Torr to ensure a low electron background and stable operation of

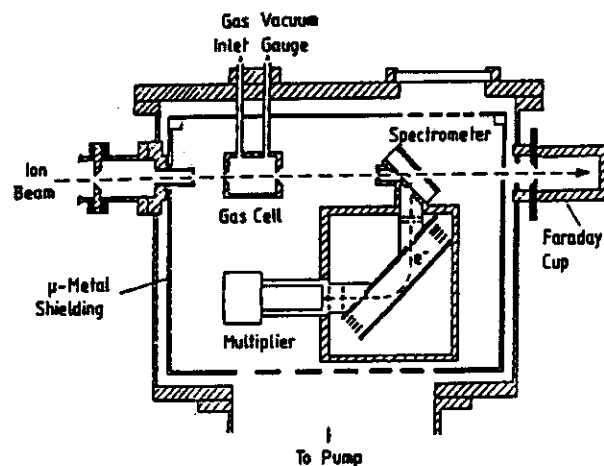


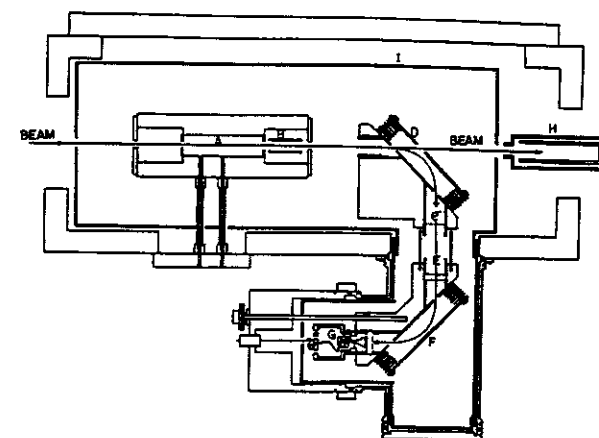
FIGURE 13.10 ZAPS set-up used at the Hahn-Meitner Institute in Berlin. Reprinted from "High resolution studies of two-electron processes observed in energetic ion-atom collisions via zero-degree Auger spectroscopy", T. J. M. Zouros, D. Schneider, and N. Stolterfoht, *Nuc. Instr. Meth. B31* (1988) 349, with kind permission of Elsevier Science - NL, Sara Burgerhartstraat 25, 1055 KV Amsterdam, The Netherlands. [22,23]

the electron detector. Typical cell apertures have diameters of $\sim 2-3$ mm. At KSU, the target cell, seen in the bottom of Fig. 13.11, is *doubly-differentially* pumped, using an extra 450 lt/s turbo-molecular pump directly on the cell. This allows for excellent running conditions with usual chamber pressures in the $1-5 \times 10^{-6}$ Torr range with target pressures in the $1-10 \times 10^{-3}$ Torr range [76,73].

It is useful to have a target cell that can be electrically floated. Then by placing a voltage on the cell, electrons produced inside the cell can be separated from electrons produced between the target cell and the spectrometer. Metastable states can thus be identified as demonstrated in Fig. 13.12.

13.3.2 The tandem electron spectrometer

ZAPS measurements to date have predominantly used the tandem spectrometer design first built by the Hahn-Meitner Institute (HMI) atomic physics group in Berlin in 1983 [22-24] and shown in Fig. 13.10. Variations of the HMI design have been used in fast collision studies at KSU [77,76] and WMU [86] and in slow-intermediate collisions at ANL [29]. Other designs have also been reported, such as a tandem composed of two spherical analyzers for 180° observation [19], a large *single-stage* hemispherical spectrometer at GSI-Darmstadt [31], a small spherical-sector spectrometer at ORNL for use with negative



**KANSAS STATE
ZERO-DEGREE TANDEM ELECTRON SPECTROMETER**

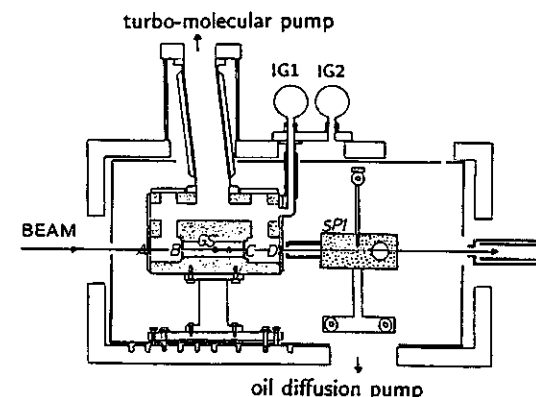


FIGURE 13.11 Kansas State University (KSU) ZAPS set-up. Top: (A) target gas cell, (B) deflector, (D) first stage used as a deflector, (E) focusing lens and retarding grids, (F) second stage used for high resolution analysis, (G) channeltron with electron suppression grid, (H) Faraday cup, (I) μ -metal shielding. Deflector (B) could be independently biased to deflect electrons when needed.

Bottom: Side view of above apparatus showing details of the double differentially pumped gas cell. This cell is pumped by a specially dedicated turbo-molecular pump directly attached to the gas cell assembly (GS) which could be electrically floated. Collimators A and D with apertures of 1.6 and 4.0 mm in diameter could also be biased independently and were used to monitor the beam. The target gas itself is kept between collimators B and C each having apertures of 2.4 mm in diameter (from Ref. [73]).

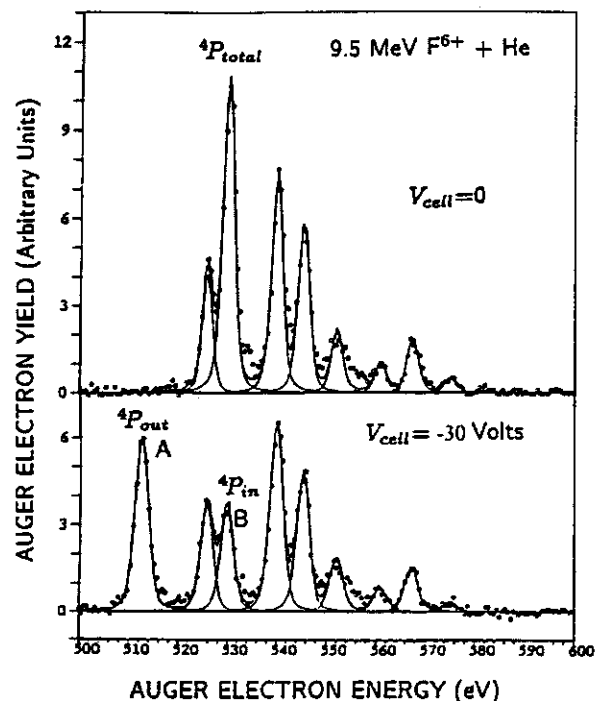


FIGURE 13.12 Identification of the metastable $1s2s2p^4P$ Auger line by biasing the target cell. Metastable states upon biasing are seen to give rise to two different lines originating from electrons produced inside (peak B) and outside (peak A) the target gas cell. The gas cell (GS) in Fig. 13.11 was biased with -30 V with respect to the spectrometer entrance slit held at ground potential. Cell collimators (A) and (D) are also held at ground potential. The electrons ejected inside the cell are thus shifted to higher energies by 30 eV in the laboratory frame. Both spectra have already been transformed back to the rest frame. In the bottom figure, the spectrum has been shifted back to its unbiased range before transforming it to the rest frame (from Ref. [73]).

ions [57] and a tandem composed of a parallel plate deflector mounted onto a hemispherical analyzer at RIKEN [33].

Principles of operation

The HMI tandem spectrometer design consists of two 45° parallel-plate analyzers connected together in series. The entrance analyzer acts as a deflector, sweeping all electrons of interest into the direction of the second analyzer where the high resolution analysis takes place. The deflector has a relatively large entrance slit to allow the ion beam to enter with the minimum of slit scatter-

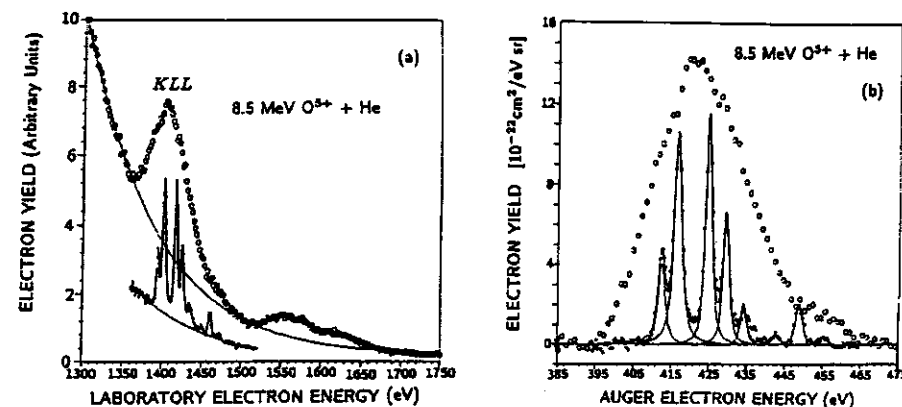


FIGURE 13.13 $O^{5+}+He$ collisions. Circles: Low resolution K-Auger spectrum taken without deceleration. Continuous line spectrum: High resolution blow up of KLL lines taken with deceleration. The structureless continuous line is a background polynomial fit. (a) Laboratory frame, (b) Projectile rest frame after background subtraction (from Ref. [73]).

ing. At zero-degrees there are many forward-scattered background electrons. The basic function of the deflector is to reduce this background.

A well known method widely used to obtain high resolution spectra is to decelerate the electrons prior to energy analysis. The instrumental energy resolution $R_{ins} = \Delta\epsilon_{ins}/\epsilon$ is a constant determined by the fixed geometry of the spectrometer [87]. Thus, by lowering the electron energy ϵ , $\Delta\epsilon_{ins}$ is also necessarily lowered. In the tandem spectrometer this is performed between the two stages. Following deceleration the electrons pass through the second analyzer with energy ϵ_{pass} . For the spectra of Fig. 13.7, taken with the HMI tandem spectrometer having a resolution $R_{ins} = 3\%$, a final $\Delta\epsilon_{ins} \sim 0.210$ eV was attained by decelerating electrons from around 175 eV down to 7 eV. This resulted in an overall resolution of $R_o = 0.210/175 = 0.12\%$. For the spectra of Fig. 13.6, taken with the KSU tandem spectrometer having a resolution $R_{ins} = 2.8\%$, electrons were decelerated down to 10 eV. This resulted in a final $\Delta\epsilon_{ins} = 0.280$ eV with a corresponding overall resolution $R_o = 0.280/216.5 = 0.129\%$.

Deceleration stage

Deceleration is produced by the two parallel high transmission grids shown in Figs. 13.10 and 13.11, just before the entrance to the second stage. These are usually separated by 2-3 mm.

The great improvement in resolution due to deceleration comes at a big cost

in transmission. The electron transmission under deceleration can be shown to be roughly proportional to the inverse of the deceleration factor, F , defined as $F \equiv \varepsilon/\varepsilon_{pass}$. Thus, large deceleration factors are usually accompanied by big losses of count rate. For this reason high beam intensities are very important.

Clearly, if $\Delta\varepsilon_{ins} \sim \Gamma_{tot}$ (where Γ_{tot} has been defined in Eq. 13.14), no substantial gain in resolution may be attained by further decreasing the pass energy. Thus, a limiting pass energy ε_{pass}^{lim} may be established and since $\Delta\varepsilon_{ins} = R_{ins}\varepsilon_{pass}$ we obtain:

$$\varepsilon_{pass} \geq \varepsilon_{pass}^{lim} = \frac{\Gamma_{tot}}{R_{ins}} \quad (13.19)$$

Values of ε_{pass}^{lim} have already been given in the example of Table 13.1.

Improvements to the electron transmission of the KSU tandem were accomplished by using a cylindrical einzel lens biased with voltage V_L as shown in Fig. 13.14. In the HMI design no extra lens is used. However, some focusing has been noted for small values of the deceleration factor. This probably results from the inherent lens properties of such a two-cylinder design [88]. Design criteria for such a deceleration system are discussed in some detail in Ref. [13].

Further improvements in the overall transmission of the HMI tandem were recently noted [89] when the entrance and exit slits of the first stage were covered with high transmission grid to reduce fringing field distortion effects [90]. The improvement in transmission is clearly demonstrated in the simulation of Fig. 13.15 produced with charge particle trajectory program SIMION [89]. It is interesting to note that no adverse effects were observed, at least at low energy collisions where this was experimentally tested, even though the entrance grid is hit by the ion beam.

Voltage scheme

Three different voltages, biasing the spectrometer plates of the entrance and exit stages, need to be scanned to record a spectrum. In Fig. 13.14, a schematic diagram of the KSU tandem spectrometer and the analyzing voltages used are shown in detail. When no deceleration is used, $\varepsilon_{pass} = \varepsilon$, V_R is grounded and only V_1 and V_2 are scanned. When decel mode is used, all three voltages V_1 , V_2 and V_R are scanned together in such a way as to maintain a fixed pass energy, ε_{pass} . The voltage scheme is given in Fig. 13.14 (left). The voltages were controlled by a computer via 12- or 16-bit digital-to-analog converters.

Spectrometer design

The 45° parallel plate analyzers were chosen for their simplicity [91,87,92,93,90]. However, this type of analyzer focuses electron trajectories in

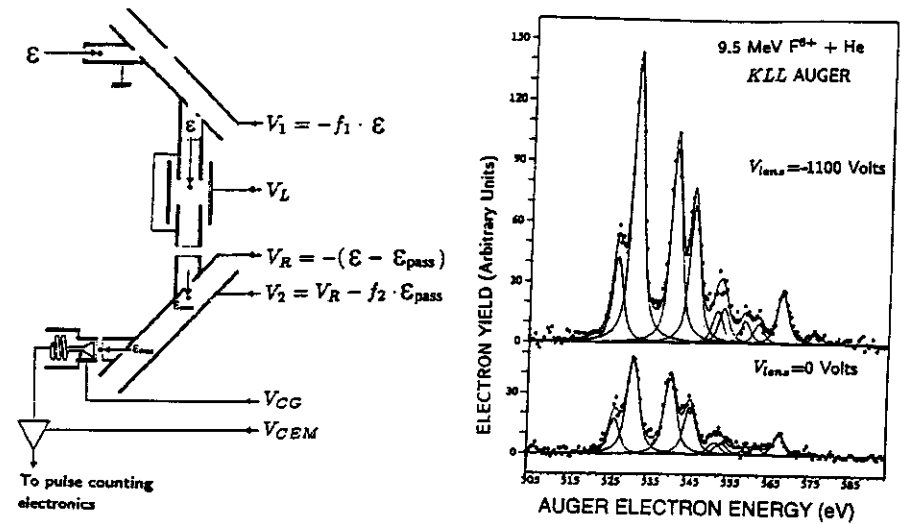


FIGURE 13.14 Left: Voltage scheme for KSU tandem electron spectrometer. Electrons enter the first stage with energy ε , are deflected by 90°, are decelerated to an energy ε_{pass} and analyzed by the second stage. On exit they are accelerated back to their original energy and detected by the channeltron. High transmission grids are placed just after the exit slit of both first and second stages to reduce field fringing. An extra grid in front of the channeltron allows for a small fixed negative voltage bias to suppress low energy electron background. The spectrometer constants f_1 and f_2 for each stage, are indicated. V_1 , V_2 and V_R were set by a computer program and stepped every time the number of ions collected in the Faraday cup reached a predetermined limit. In deceleration mode, ε_{pass} is fixed thus maintaining a constant transmission through the second stage. In non-deceleration mode, $\varepsilon_{pass} = \varepsilon$ and $V_R = 0$, resulting in a transmission that depends on the energy ε . The einzel lens voltage V_L was set empirically for maximum transmission and left constant under deceleration operation. Its effect is shown in the spectra on the right. Right: Einzel lens performance under deceleration operation. Here, $\varepsilon_{pass} = 150$ eV and the mean laboratory energy, $\bar{\varepsilon} = 1600$ eV. Thus, the overall deceleration factor is $F \sim 10.7$. The lens is seen to increase the yield by a factor of 2.5 (figures adapted from Ref. [73]).

only one direction and only to first order [87,92]. Higher transmission can be attained by hemispherical analyzers [94–96,90,92] which are double-focusing, but have yet to be used extensively in zero-degree studies. We shall not go into the details of spectrometer design and their focusing properties but refer the reader to the many existing reviews and articles [87,94–96,92,90,97]. Both HMI and KSU tandem spectrometers were made out of brass for HV operation, with an aluminum version of the HMI spectrometer fabricated for UHV operation. High quality insulators with low outgassing rates such as Vespel (polyimide) or Delrin are used in the construction [90]. Guard electrodes

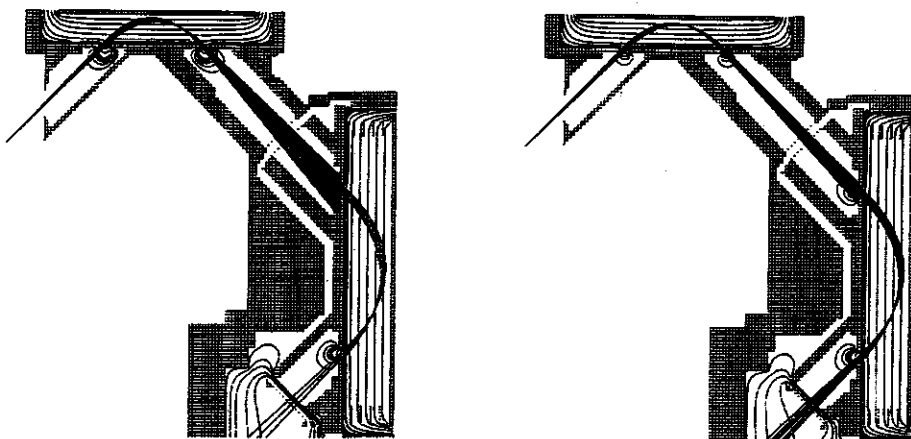


FIGURE 13.15 Effect of fringing fields around the slits of the first stage of the HMI tandem spectrometer. No deceleration is used. The electron trajectories are shown leaving from the source at the upper left, traversing the two 45° parallel plate analyzers and finally detected on the bottom right of each figure. Left: Strong fringing field—no grid is used. Right: Weak fringing field produced by placing a high transmission grid on both slits. When the fringing field is reduced improved transmission results. The simulation was performed with program SIMION. The electron energy is 1 keV. The equipotential lines are clearly shown indicating the fringing fields [89].

were utilized particularly on the second stage to further compensate for field distortion caused by fringing.

In Table 13.2 typical values of various spectrometer parameters for both the KSU and HMI tandem designs are listed for comparison. The basic equations for computing these parameters are also given in the table. In calculating the acceptance angles it is assumed that the length of the electron trajectory between foci does not contribute. Thus, distances along the parabolic trajectories from entrance to exit slits in each analyzer are not included in the calculation of $\Delta\phi$, since in this direction there is first-order focusing, while they are included in the calculation of $\Delta\theta$ where there is no focusing. The length $1.148l_i$ is the length of the parabolic trajectory in stage i between slits separated by length l_i with $i = 1$ or 2.

As seen in Table 13.2, the biggest difference between the two spectrometers is the much larger separation between stages in the KSU design as well as the much larger gas cell (midpoint) distance to the spectrometer (y_c). Thus, the HMI design is seen to be very compact with a 6 times larger effective solid angle. The KSU spectrometer, however, with its reduced acceptance angle has a correspondingly smaller kinematic broadening and the longer electron flight paths help to further reduce background from stray electrons. Furthermore,

TABLE 13.2 Design parameters of the KSU [76] and HMI [22] tandem 45° parallel-plate spectrometers. All lengths are in mm. Lengths in the HMI set-up vary depending on whether intermediate (10–150 keV/u) or high (3–5 MeV/u) energy collisions are studied.

Parameter	KSU		HMI		Definition
	stage 1	stage 2	stage 1	stage 2	
slit separation (l)	69	69	35	50	center-to-center
entrance slit width (w^i)	3.3	2.5	4	1.5	
entrance slit length (t^i)	4.7	9.9	10	10	
exit slit width (w^o)	4.7	1.3	4	1.5	
exit slit length (t^o)	10	9.8	10	10	
field plate separation (d)	21.8	21.2	10.5	15	$f = \frac{2d}{t}$
spectrometer constant (f)	0.63	0.614	0.6	0.599	
Resolution: $R = \Delta\epsilon/\epsilon$					
Base (R_B)	11.6%	5.6%	23.0%	6.0%	$R_B = \frac{w^i + w^o}{t} + 2(\Delta\phi/2)^2 + \frac{1}{2}(\Delta\theta/2)^2$
FWHM (R_{ins})	5.8%	2.8%	11.5%	3.0%	
distance between stages (S)	120		54		exit slit 1–entrance slit 2
gas cell length (l_c)	100		50 (100)		
gas cell distance (y_c)	202		95 (120)		cell mid-point–entrance slit 1
Point-source					
Full acceptance angles (°):					Point-source at y_c $\Delta\phi = \frac{w_0^2}{\sqrt{2}(y_c + S)}$ $\Delta\theta = \frac{t_0^2}{y_c + S + 1.148(l_1 + l_2)}$ $\Delta\Omega_0(y_c) = \Delta\theta\Delta\phi$
Focusing direction ($\Delta\phi$)	0.17		0.41 (0.35)		
Non-focusing direction ($\Delta\theta$)	1.17		2.3 (2.1)		
Solid angle ($\Delta\Omega_0$ in μSr)	59		289 (225)		

the large gas cell pressures that could be used due to the double-differential pumping of the cell somewhat compensated for the loss in solid angle.

Electron detectors

The energy-analyzed electrons can be detected using various types of detectors. The HMI spectrometer has been used primarily with a high gain electron multiplier. This detector provides a rather energy-independent electron detection efficiency η , has a large detection area and can be run at high count rates (~ 500 kHz). The main drawback of this detector, however, is that it has to be kept constantly under vacuum to avoid serious efficiency degradation. The KSU spectrometer uses a channeltron detector. It also has a high efficiency $\eta \sim 0.5 - 0.8$, but has a smaller detection area and a smaller maximum count rate (~ 100 kHz). Channeltrons can remain in the open air without any problem when not in operation. Channel plates have also been used [98–100], enjoying most of the advantages of both multiplier and channeltron detectors. However, their higher dark current and greater fragility seems to have somewhat discouraged their use to date. In future more efficient devices, utilizing position sensitive detection, channel plates can be expected to play a dominant role.

The independent efficiency calibration of electron detectors is rather tedious and somewhat controversial. [101] In electron spectroscopy measurements most cross sections are normalized to known absolute target Auger electron standards. The authors have developed a different technique to measure the overall efficiency by *in situ* measurements of the Binary Encounter electron (BEE) peak [102] and normalization to well-accepted *calculated* BEE cross sections. This method is described in detail in the next section.

13.4 DATA ANALYSIS-SELECTED TOPICS

Here we discuss particular aspects of ZAPS data analysis related to absolute cross section determination of prompt and metastable states. These topics have not received much attention previously.

13.4.1 Absolute cross section determination: Binary Encounter peak method

The laboratory double-differential cross section (DDCS) for electron production are given in general by: [8,103]

$$\frac{d^2\sigma}{d\epsilon d\Omega} = \frac{N^e}{N_0 n T(\epsilon) l_c \Delta\Omega \Delta\epsilon \eta(\epsilon)} \quad (13.20)$$

where $N^e = N^e(E_p, \epsilon, \theta)$ is the measured electron count at a particular collision energy E_p , electron energy ϵ and detection angle θ . n and l_c are the target gas density and the gas cell length. $\Delta\Omega$ is the effective solid angle. For prompt states, $\Delta\Omega$ is the just the point source solid angle $\Delta\Omega_0(y_c)$ for a source at a distance y_c from the spectrometer entrance slit as given in Table 13.2. For long lived states, the electrons can be ejected at any point along the path after the collision in the target cell and a more elaborate calculation for $\Delta\Omega$ is required. This is presented in section 13.4.2. The transmission $T(\epsilon)$ is the overall transmission of the electron spectrometer and $\eta(\epsilon)$ is the intrinsic electron detector efficiency. The energy band-pass of the spectrometer, is $\Delta\epsilon = R_{ins} \epsilon$. In deceleration mode $\epsilon = \epsilon_{pass}$, (see section 13.3.2) and thus is constant. R_{ins} , the instrumental energy resolution of the high resolution stage of the spectrometer is also a constant. N_0 is the number of incident projectiles.

In the special case where the beam of incident particles has a strong metastable component which contributes to some or all of the observed Auger lines (as for example in the case of Be-like O^{4+} beams having almost 60% of the projectiles in the $1s^2 2s 2p^3 P$ metastable state), Eq. 13.20 will not in general be correct [8]. However, Eq. 13.20 may still be used to define the normalized double differential yield (NDDY). The NDDY must then be multiplied

by a correction factor to give the DDCS. These corrections are discussed in sections 13.4.2 and 13.5.1.

Assuming $N_0, n, l_c, \Delta\Omega_0(y_c), R_{ins}$ and ϵ are well known, $T(\epsilon)$ and η are the most important parameters to determine. These can be obtained through careful experimentation or may be deduced by comparison to accepted cross section "standards". Even in the later case, these standards are only known for some particular energy or angular ranges and thus the need to extrapolate to a different range might introduce various new assumptions and errors.

We present a method [102,38] for determining the product $T(\epsilon)\eta$ in ZAPS by normalizing electron DDCS to *calculated* Binary Encounter electron (BEE) DDCS produced in collisions of *bare ions* with H_2 or He targets [102]. This method is particularly well suited to zero-degree observation in energetic collisions and has the advantage that it provides a direct and accurate *in situ* absolute calibration (normalization) of the overall efficiency $T(\epsilon)\eta$ over a large electron energy range $\epsilon \sim 1 - 5$ keV.

Binary Encounter electrons [102] are target electrons ionized through direct, hard collisions with energetic projectiles, giving rise to a broad energy distribution centered approximately at a laboratory electron energy $\sim 4t\cos^2\theta$ [104,14]. The BEE DDCS are well described in the impulse approximation (IA) for $\theta = 0^\circ$ observation [102]. As seen from the projectile frame, the target electron suffers a 180° Rutherford scattering off the ion with cross section $(\frac{d\sigma}{d\Omega})_R$ [102]. Thus, the following simple formula, obtained in the IA, gives the laboratory BEE DDCS (in a.u.), for collisions of *bare ions* with H_2 and He targets for $\theta = 0^\circ$: [102]

$$\left(\frac{d^2\sigma}{d\epsilon d\Omega}\right)_{BEE} = \left(\sqrt{\frac{t}{\epsilon'}} + 1\right) \left(\frac{d\sigma}{d\Omega'}\right)_R \frac{J(p_z)}{\sqrt{2t + p_z}} \quad (13.21a)$$

where

$$\left(\frac{d\sigma}{d\Omega'}\right)_R = \frac{Z_p^2}{16\epsilon'^2} \quad (13.21b)$$

$$p_z = \sqrt{2}(\sqrt{\epsilon' + \epsilon_I} - \sqrt{t}) \quad (13.21c)$$

$$\epsilon = (\sqrt{t} + \sqrt{\epsilon'})^2$$

Thus, $\left(\frac{d^2\sigma}{d\epsilon d\Omega}\right)_{BEE}$ and the laboratory electron energy ϵ are given as functions of ϵ' . $J(p_z)$ is the Compton profile of the target electron, representing the probability of finding such an electron with momentum p_z along the z-axis taken along the collision direction. The Compton profile for H_2 or He is experimentally known and given analytically [105]. The ionization energies ϵ_I are 15.5 and 24.5 eV for H_2 and He, respectively. The BEE DDCS formula as given by Eqs. 13.21 is very convenient and simple to use and has been found to be in excellent agreement with measured DDCS in a variety of collision systems for bare ions with $Z_p = 1 - 9$ [102]. The validity of the IA description

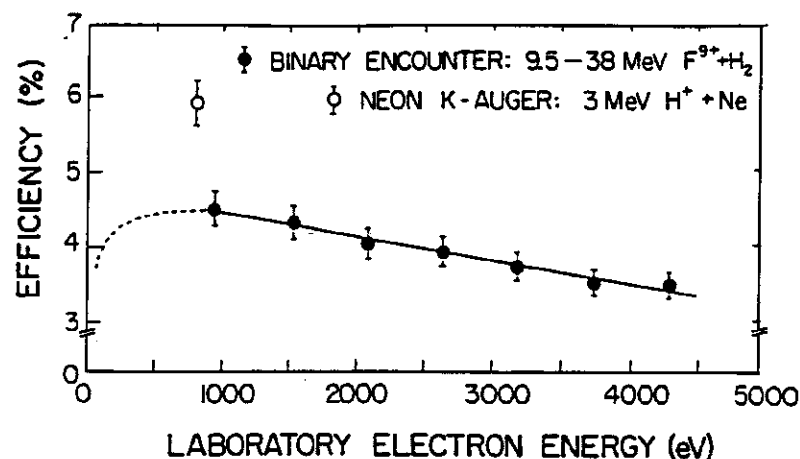


FIGURE 13.16 Overall absolute spectrometer efficiency $T(\epsilon)\eta$ plotted as a function of the laboratory electron energy ϵ . The solid line was interpolated using the data points (solid circles) obtained by normalizing the $F^{9+} + H_2$ BEE yields to the IA calculation (see text). The dashed line was extrapolated using the results of Ref. [111]. The open circle is the efficiency measured using the known Ne target K-Auger cross section [112] at $\epsilon \approx 800$ eV for 3 MeV $H^+ + Ne$ collisions. The error bars are calculated from statistics alone. The Ne K-Auger data have an overall absolute uncertainty of 20% [112] (adapted from Ref. [73]).

of the BEE peak is also supported by more sophisticated calculations based on the CDW-EIS formulation, in which two-center effects due to the influence of both the projectile and target charges on the ejected electrons are included [106,107].

For partially stripped ions ($q \neq Z_p$) the BEE DDCS can still be calculated by the above simple formula [108] but the Rutherford cross section needs to be replaced by the cross section for elastic scattering in the field of a *non-bare* ion requiring a more elaborate calculation [109,110]. In this case, BEE DDCS are known to *increase* with decreasing charge-state q [108].

By comparing the IA calculation of Eq. 13.21 to *measured* BEE DDCS, $T(\epsilon)\eta$ is directly determined for $\epsilon \sim 3t - 5t$ around the BEE peak. By varying the collision energy (t), a much larger electron energy range can be covered. The overall efficiency $T(\epsilon)\eta$ determined in this way is shown as a function of ϵ in Fig. 13.16 for the KSU spectrometer [102].

When high resolution spectra (from partially stripped ions) are obtained using deceleration in the tandem spectrometer, further loss of transmission occurs and $T(\epsilon_{pass}, F)$ must be determined, where $F = \epsilon/\epsilon_{pass}$ is the deceleration factor. This can in principle be accomplished as discussed above by directly measuring bare BEE DDCS in *deceleration* mode. However, in

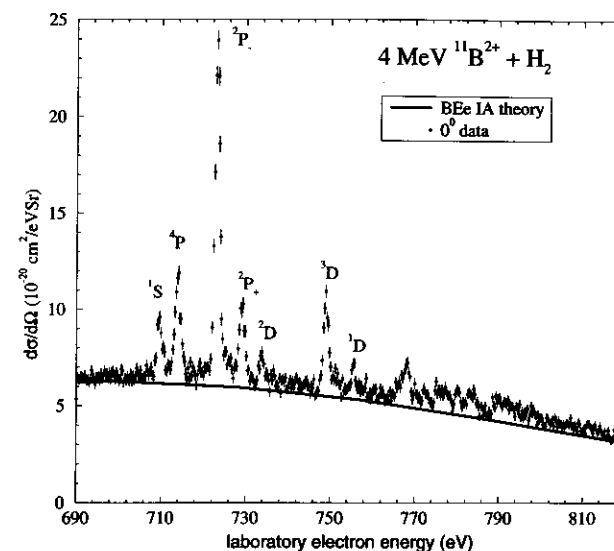


FIGURE 13.17 High resolution 0° data from 4 MeV $B^{2+} + H_2$ collisions [113]. The Auger DDCS have been converted to an absolute scale by *normalizing* to calculated BEE DDCS for $B^{2+} + H_2$ collisions, which have in turn been scaled from bare $B^{5+} + H_2$ BEE DDCS, as described in the text.

practice, since beam currents can be small for bare ions this method may be impractical. In this case, a slightly different procedure is followed:

- BEE DDCS $(\frac{d\sigma}{d\epsilon d\Omega})_{q=Z_p}$ for *bare* ions are measured in *low* resolution and compared to calculated IA BEE DDCS, thus determining the product $T(\epsilon)\eta$ as already discussed [102].
- BEE DDCS $(\frac{d\sigma}{d\epsilon d\Omega})_q$ for *partially-stripped* ions of charge-state q , are measured in *low* resolution and converted to absolute DDCS using the value of $T(\epsilon)$ determined in (a). The overall efficiency $T(\epsilon)\eta$ should be the same as in (a) since it depends only on the electron energy which is the same for both cases (a) and (b) [108].
- High resolution DDCS, for the ion of charge-state q is now measured using deceleration. The measured spectrum includes Auger lines superimposed on the BEE peak determined in (b) as shown in Fig. 13.17. Thus, by normalizing the high resolution DDCS to the absolute BEE DDCS determined in (b), $T(\epsilon_{pass}, F)$ is fixed and the final *absolute* DDCS may be obtained in the laboratory frame.

This method of absolute normalization is limited to fairly fast collisions ($E_p > 0.5$ MeV/u) for which the BEE peak is well separated from the Cusp

TABLE 13.3 Lifetimes τ_J (ns) of the $1s2s2p^4P$ state for light ions.

Ion	$J = \frac{1}{2}$	$J = \frac{3}{2}$	$J = \frac{5}{2}$	References
He ⁻	10.7 μ s	12 \pm 2 μ s	350 \pm 15 μ s	[116,117]
C ³⁺	3.69	13.2	117	[118]
O ⁵⁺	0.91	3.34	27.67	[118]
F ⁶⁺	0.57	1.84	15.90	[118]
Ne ⁷⁺	0.40	1.6	10.4	[119]

peak. Furthermore, it relies on the availability of intense bare ion beams not always available at the projectile energy of interest. Typical minimum beam currents with light ions are $\sim 5 - 10$ nA for low resolution BEE studies and $\sim 50 - 100$ nA for high resolution work. For less intense beam currents more conventional normalization methods can be used with some care to obtain absolute DDCS for non-bare ions, including direct comparisons to theoretical BEE DDCS of *partially* stripped ions. Studies of BEE DDCS for few-electron projectiles are still under active investigation. [108–110,114,115] For collisions with H₂ and He, theory seems to be in good agreement with experiment for few-electron ions [109,110]. In general, more work is needed in establishing reliable absolute standards for DDCS at zero-degrees.

13.4.2 Single differential cross section determination of long-lived states

Upon integrating the DDCS given by Eq. 13.20 over the electron energy for each Auger line (e.g. area under the peak) one obtains the single differential cross section (SDCS). In the case of long-lived projectile Auger states one faces the additional difficulty that part of the measured yield N^e originates outside the target cell along the path between the cell and the spectrometer resulting in a very different effective solid angle than in the case of prompt Auger transitions. This has been demonstrated in Fig. 13.12. For such a metastable state, we may set the effective solid angle, $\Delta\Omega$ (see Eq. 13.20), equal to $G_\tau \Delta\Omega_0(y_c)$ and compute the correction factor G_τ .

The most commonly encountered metastable state in ZAPS is the $1s2s2p^4P$ state. Lifetimes τ_J depend on the total angular momentum component J and are given in Table 13.3 for a few light ions. For the Li-like oxygen and fluorine 4P states in 0.5–2 MeV/u collisions the effect of the long lifetimes gave $G_\tau \sim 1.5 - 1.7$ showing this to be a substantial correction [73]. Typical decay curves are shown in Fig. 13.18 for 4–32 MeV collisions of O⁵⁺. We note that for low- Z ions, the different J components of the Auger line cannot usually be resolved.

The correction factor G_τ is computed as follows. The number of projectiles excited to the metastable state J in collisions with a differential target length

element dx is:

$$dN_0^J = N_0 n \sigma_J dx \quad (0 \leq x \leq l_c) \quad (13.22)$$

where σ_J is the *production* cross section for populating state J in the collision. Within the time $t = y/V_p$ and $t + dt$ later, $dN^J(y)$ metastable states decay:

$$dN^J(y) = dN_0^J \frac{e^{-y/V_p \tau_J}}{V_p \tau_J} dy \quad (0 \leq y \leq L - x) \quad (13.23)$$

where $L = y_c + l_c/2$ is the distance from the cell entrance to the spectrometer entrance slit. Defining $\frac{dw_J}{d\epsilon d\Omega} \xi_J$ as the double differential probability for electron emission into the direction (θ, ϕ) with energy ϵ and Auger yield ξ_J , we integrate all contributions along the beam trajectory in front of the spectrometer to obtain the total detected yield, N_J^e , as follows:

$$N_J^e = N_0 n \sigma_J \frac{dw_J(\theta = 0^\circ)}{d\epsilon d\Omega} \xi_J l_c G_\tau \Delta\Omega_0(y_c) \Delta\epsilon T(\epsilon) \eta(\epsilon) \quad (13.24)$$

with

$$G_\tau \equiv \left[\frac{1}{l_c \Delta\Omega_0(y_c)} \int_{x=0}^{l_c} dx \int_{y=0}^{L-x} dy \frac{e^{-y/V_p \tau_J}}{V_p \tau_J} \Delta\Omega_0(L - x - y) \right] \quad (13.25)$$

where we have assumed for simplicity that $\frac{dw_J}{d\epsilon d\Omega}$ does not vary much along the integration path.

We note that $\sigma_J \frac{dw_J(\theta=0^\circ)}{d\epsilon d\Omega} \xi_J$ can be identified with the DDCS of Eq. 13.20 for the particular state component J . Adding all J contributions we obtain:

$$N^e = \sum_J N_J^e = N_0 n l_c \Delta\Omega_0(y_c) \Delta\epsilon T(\epsilon) \eta \sigma \frac{dw}{d\epsilon d\Omega} \sum_J a_J \xi_J G_\tau \quad (13.26)$$

In Eq. 13.26 we have assumed statistical production of the states J with $\sigma_J = a_J \sigma$, where σ is the total production cross section (for all J states) and a_J the statistical weight with $a_J = (2J + 1) / \sum_J (2J + 1)$. We have also assumed that w_J does not depend strongly on J and set $w_J = w$. If we use the J -averaged Auger yield $\xi \equiv \sum_J a_J \xi_J$, we obtain from Eq. 13.26 the averaged value for G_τ :

$$G_\tau = \frac{\sum_J (2J + 1) \xi_J G_\tau}{\sum_J (2J + 1) \xi_J} = \frac{\sum_J a_J \xi_J G_\tau}{\xi} \quad (13.27)$$

It is seen, that in the limit $V_p \tau_J \rightarrow 0$ (prompt states) and $l_c \rightarrow 0$ (point source) $G_\tau = 1$ as expected.

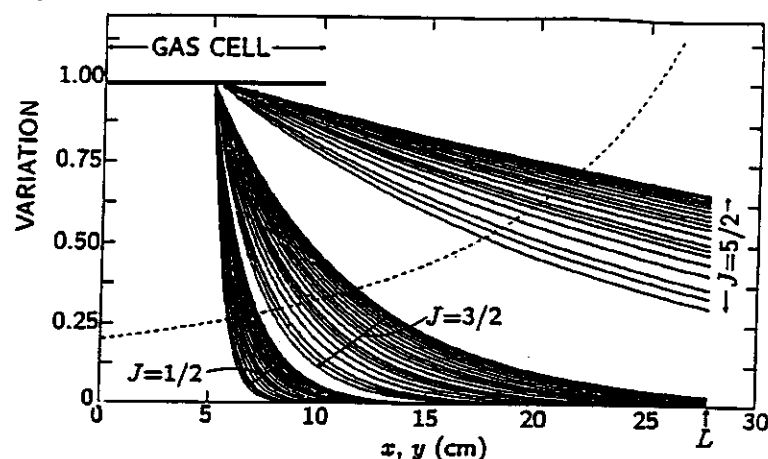


FIGURE 13.18 Decay curves, $e^{-y/V_p\tau_j}$ for the $O^{5+}(1s2s2p)^4P_J$ states (assumed to be produced at the center of the gas cell) for different projectile energies ranging from 4–32 MeV. A large part of the states are seen to decay outside the target cell volume, some even beyond the spectrometer. The dashed line shows the variation of solid angle $\Delta\Omega_0(y)$ as a function of y from $y = 0$ to $y = L$. The spectrometer entrance is at L (adapted from Ref. [73]).

13.5 PRACTICAL APPLICATIONS

13.5.1 Determination of metastable beam fractions in Be-like beams

The method of ZAPS has been used to determine the metastable beam fraction, F_m , of the long-lived $1s^2 2s 2p^3 P$ state in Be-like C^{2+} , O^{4+} [8] and Ne^{6+} [27] ions, in collisions with H_2 and He. The basic premise underlying the determination of F_m is that the cross section for $1s$ ionization of the ground state $1s^2 2s^2 1S$ is the *same* as that for the metastable state $1s^2 2s 2p^3 P$. This premise, experimentally verified in high resolution K x-ray studies, has been used before in the determination of the metastable beam fraction of He-like ions [85]. The K -shell ionization cross section σ_K^g and σ_K^m of the ground and metastable states, respectively, are assumed to be equal, i.e. $\sigma_K^g = \sigma_K^m$, if the ionization process is unaffected by differences in the outer shell configurations. In this case, “needle” ionization conditions apply, as already discussed in section 13.2.2 for collisions with light targets such as H_2 and He.

Schematically, if T represents the target (He or H_2) and P the Be-like projectile of charge-state q , for $1s$ ionization of the ground state followed by Auger relaxation we have:

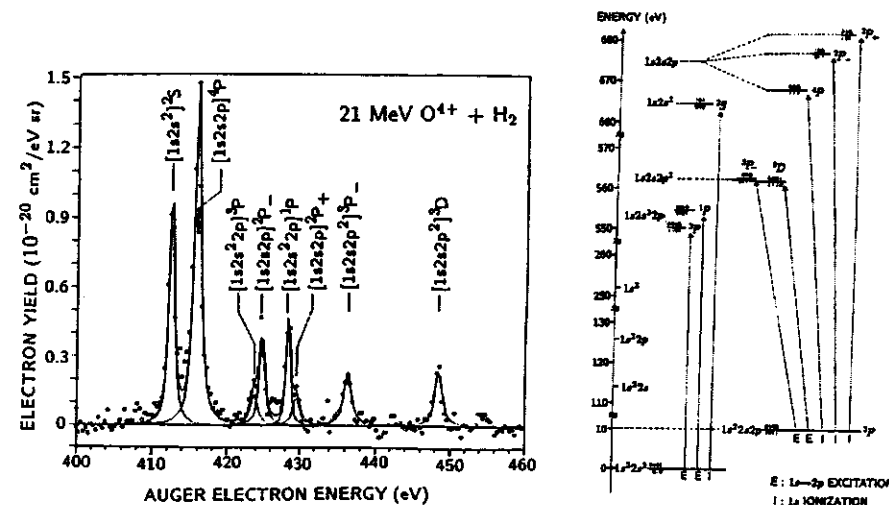
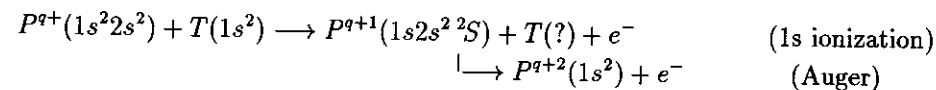
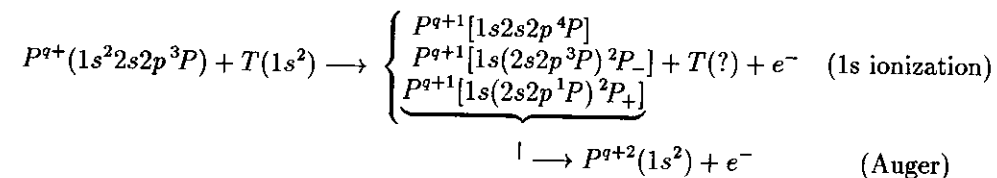


FIGURE 13.19 Normalized zero-degree Auger electron yield for 21 MeV O^{4+} collisions with H_2 after subtraction of background continuum electrons and transformation to the projectile frame. The $1s2s^2\ ^2S$ line results from $1s$ ionization of the ground state. The $4P$, $^2P_-$ and $^2P_+$ states result from $1s$ ionization of the metastable $1s2s2p^3\ ^3P$ ion. All other lines are due to the decay of Be-like configurations produced by excitation. The transition scheme is given on the right (from Ref. [73]).



In the case of $1s$ ionization of the metastable state, however, the metastable ion, upon losing a $1s$ electron, can autoionize giving rise to the three distinct lines in the electron spectra [44], as shown in Fig. 13.19:



The cross sections σ_K^g and σ_K^m can be directly determined from the NDDY, $dY/d\Omega$, measured for each of the four states using Eq. (13.20):

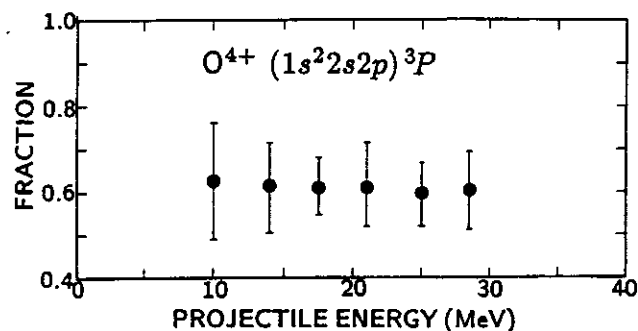


FIGURE 13.20 Metastable ($1s^2 2s 2p^3P$) beam fraction in energetic $O^{4+} + He$ and H_2 collisions determined by ZAPS (adapted from Ref. [8]).

$$\sigma_K^g = \left(\frac{N_0}{N_g} \right) \frac{4\pi}{\xi_{2S}} \frac{dY(^2S)}{d\Omega} = \frac{4\pi}{F_g} \frac{1}{\xi_{2S}} \left[\frac{dY(^2S)}{d\Omega} \right] \quad (13.28)$$

$$\sigma_K^m = \left(\frac{N_0}{N_m} \right) \sum_X \frac{4\pi}{\xi_X} \frac{dY(X)}{d\Omega} = \frac{4\pi}{F_m} \left[\frac{1}{\xi_{4P}} \frac{dY(^4P)}{d\Omega} + \frac{1}{\xi_{2P_-}} \frac{dY(^2P_-)}{d\Omega} + \frac{1}{\xi_{2P_+}} \frac{dY(^2P_+)}{d\Omega} \right] \quad (13.29)$$

where ξ_X is the Auger yield of state X . F_g and F_m are the beam fractions in the ground or metastable state, respectively. It is seen that $\frac{4\pi}{\xi_X} \frac{dY(X)}{d\Omega}$ are the *state production* yields, determined by integrating the NDDY given in Eq. 13.20 over electron energy (i.e. area under the peak for each state X) and emission angle, assuming isotropic emission.

Equating Eqs. (13.28) and (13.29) and using $F_g + F_m = 1$ we may solve for F_m to obtain:

$$F_m = \frac{\left[\frac{1}{G_r \xi_{4P}} \frac{dY(^4P)}{d\Omega} + \frac{1}{\xi_{2P_-}} \frac{dY(^2P_-)}{d\Omega} + \frac{1}{\xi_{2P_+}} \frac{dY(^2P_+)}{d\Omega} \right]}{\left[\frac{1}{\xi_{2S}} \frac{dY(^2S)}{d\Omega} + \frac{1}{G_r \xi_{4P}} \frac{dY(^4P)}{d\Omega} + \frac{1}{\xi_{2P_-}} \frac{dY(^2P_-)}{d\Omega} + \frac{1}{\xi_{2P_+}} \frac{dY(^2P_+)}{d\Omega} \right]} \quad (13.30)$$

The correction for the long lifetime of the $(1s 2s 2p)^4P$ state is seen to be explicitly included in G_r [120]. More details, including comparisons to a different method based on the coefficients of fractional parentage of the states can be found in Ref. [8].

The experimentally determined fraction F_m , using Eq. (13.30), is shown in Fig. 13.20 for O^{4+} projectiles. Both He and H_2 targets gave very similar results and thus only the average for both targets is shown. F_m is seen to be fairly constant within the experimental error over the whole range of projectile energies, consistent with other similar determinations [27,85].

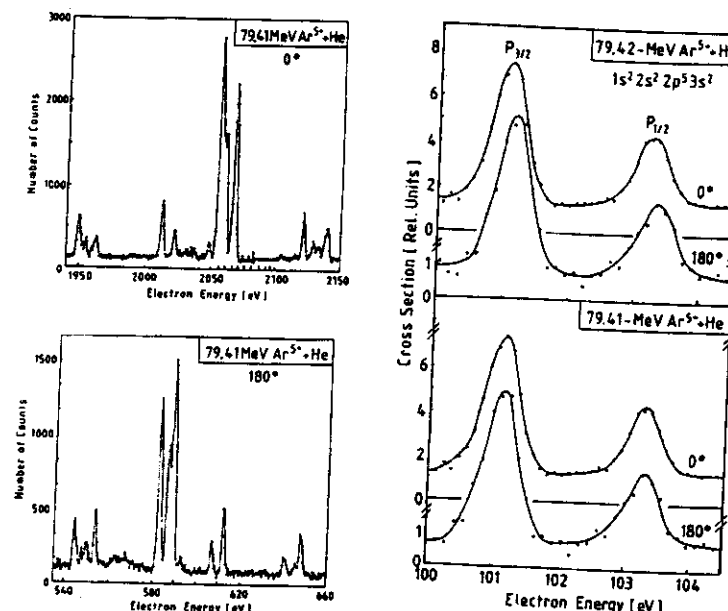


FIGURE 13.21 Ar-L-Auger spectra from collisions of Ar^{5+} with He. Left: Laboratory spectra correspond to rest frame ejection angles $\theta' = 0^\circ$ (top) and 180° (bottom). Right: Projectile rest frame spectra. When a projectile energy of 79.42 MeV is chosen a slight mismatch between the rest frame lines is observed (top). However, when an energy of 79.41 MeV is used (bottom) good agreement is obtained. Reprinted from N. Stolterfoht, "High-resolution Auger spectroscopy in energetic ion atom collisions" [27], with permission.

13.5.2 Determination of the projectile beam energy—Accelerator energy calibration

The Auger line energies can be accurately determined only if the projectile energy is also accurately known. If t and ε are known, then the Auger energy ε' can be directly obtained via Eq. 13.1a. Measured laboratory electron energies have a relative uncertainty of $\sim 0.1 - 0.3$ eV. By taking a high resolution scan of the Cusp energy region a very good determination of t can be obtained. This method can be used to calibrate the energy of accelerators with the same or superior accuracy than possible with more conventional techniques [121,122].

In cases where both the forward (+) and backward (-) laboratory electron energy lines ε_{\pm} can be observed (energy doubling), only possible for $t > \varepsilon'$ (see example in Fig. 13.6), a different method can be used to accurately determine both t and ε' , via Eq. 13.4a. This is demonstrated in Fig. 13.21 where the projectile velocity is adjusted until the corresponding Auger lines coincide in

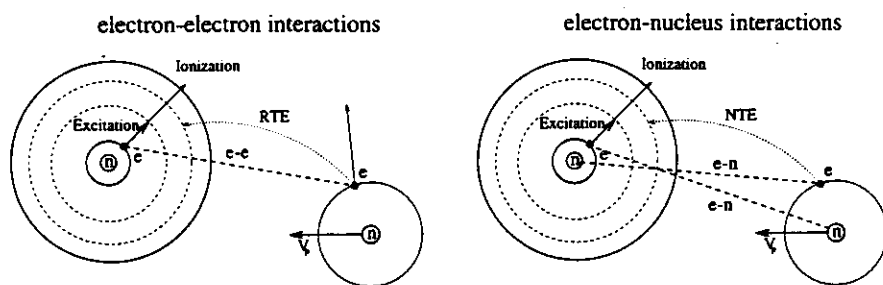


FIGURE 13.24 Projectile excitation can be mediated either through electron-electron (e-e) interactions (left) or electron-nucleus (e-n) interactions (right). Left: The target *electron* interacts with the projectile electron, either exciting it to a discrete (e-e Excitation) or continuum state (e-e Ionization). In the case where excitation is accompanied by simultaneous capture of the exciting target electron the process is known as Resonance Transfer Excitation (RTE). In e-e interactions the excitation of both electrons is correlated and the target is always excited or ionized. In the limit where the target electron can be considered to be *free*, these processes would correspond to the electron-ion scattering processes of electron impact Excitation, Ionization and Dielectronic Capture, respectively. Right: The target *nucleus* interacts with the projectile electron either exciting it to a discrete (e-n Excitation), or continuum state (e-n Ionization). In the case where excitation is accompanied by simultaneous capture of an electron the process is known as Non resonance Transfer Excitation (NTE). During e-n interactions, the excitation of the projectile is independent of the final state of the target electron, which usually remains in the ground state.

TABLE 13.4 Collision processes linked via the impulse approximation (IA)

Ion-Atom collision processes	↔ IA	Electron-Ion collision processes
Resonance Transfer Excitation (RTE)	↔	Dielectronic Capture (DC) or time-reversed Auger
e-e Excitation (eeE)	↔	electron Impact Excitation (eIE)
e-e Ionization (eeI)	↔	electron Impact Ionization (eII)
Binary Encounter electrons (BEe)	↔	Elastic electron Scattering

In general both e-e and e-n interactions are present simultaneously during the collision both giving rise to the same excited projectile state. Thus, signatures have to be discovered by which the e-e contributions can be identified over and above the usually stronger e-n contributions. We note that Eq. 13.31 gives the cross section *only* for the e-e interaction. The usually competing e-n interaction may be computed independently, within a Born treatment and just added to the e-e cross section. New theoretical approaches are becoming available in which both e-e and e-n interactions are included in a four-body

theory and their contributions are added coherently, with the possibility of interference [134,135]. In other cases, the e-n “background” can be almost completely eliminated by a judicious choice of the experimental parameters [11]. In the following sections the different e-e signatures are demonstrated from recent results using ZAPS.

Resonance Transfer Excitation (RTE)

The *free* electron analogue of RTE is the time-reversed Auger effect, also known as dielectronic capture (DC). It is reminded that a free electron cannot be captured without losing energy. In dielectronic capture, this energy is lost to projectile excitation. Excitation to a particular projectile state requires exactly the right amount of energy and therefore this process is highly resonant. This can also be seen from the principle of detailed balance applied to the time-reversed Auger process. Thus, the cross section for dielectronic capture is well approximated by a delta-function in the electron collision energy ϵ' with $\sigma_{DC} \sim \delta(\epsilon' - \epsilon_A)$, ϵ_A being the Auger energy of the particular doubly-excited state of the projectile formed by dielectronic capture. Substituting σ_{DC} for σ_{eI} in Eq. 13.31 and performing the now trivial integration over the energy profile of the “beam” of target electrons we obtain (in a.u.):

$$\sigma_{RTE} \sim \frac{J(p_z)}{\sqrt{2t + p_z}} \quad (13.32a)$$

$$p_z = \sqrt{2}(\sqrt{\epsilon_A + \epsilon_I} - \sqrt{t}) \quad (13.32b)$$

Since $J(p_z)$ is maximum for $p_z = 0$ it is seen that at $t = (\epsilon_A + \epsilon_I)$, σ_{RTE} will be a maximum. Thus, RTE is seen to have a resonance at $E_p = \frac{M_p}{m}(\epsilon_A + \epsilon_I)$.

The doubly excited projectile state produced by RTE can decay back down to the ground state either by photon or Auger electron emission. Thus, the RTE resonance signature may be observed in the collision energy dependence of characteristic X rays or Auger electrons of the projectile. A resonance, at the predicted energy would verify RTE. The first observation of an RTE resonance in 1982 used K X rays in coincidence with projectile ions whose charge state was reduced by one due to electron transfer [136,137]. However, the X rays were measured in low resolution and thus more than one state could contribute. Just a few years later ZAPS provided the first *state-selective* measurements [23,35–38,138–140] of RTE. Some of these results are shown in Fig. 13.25. The RTE resonance for the Be-like fluorine $3D$ state occurs around 20 MeV and is formed by $1s \rightarrow 2p$ excitation and capture to a $2p$ orbital. The Auger energy for this state is 567.8 eV, as seen from the Auger spectrum on the left. We note that by using H_2 as a target, e-n contributions due to NTE were minimized [37].

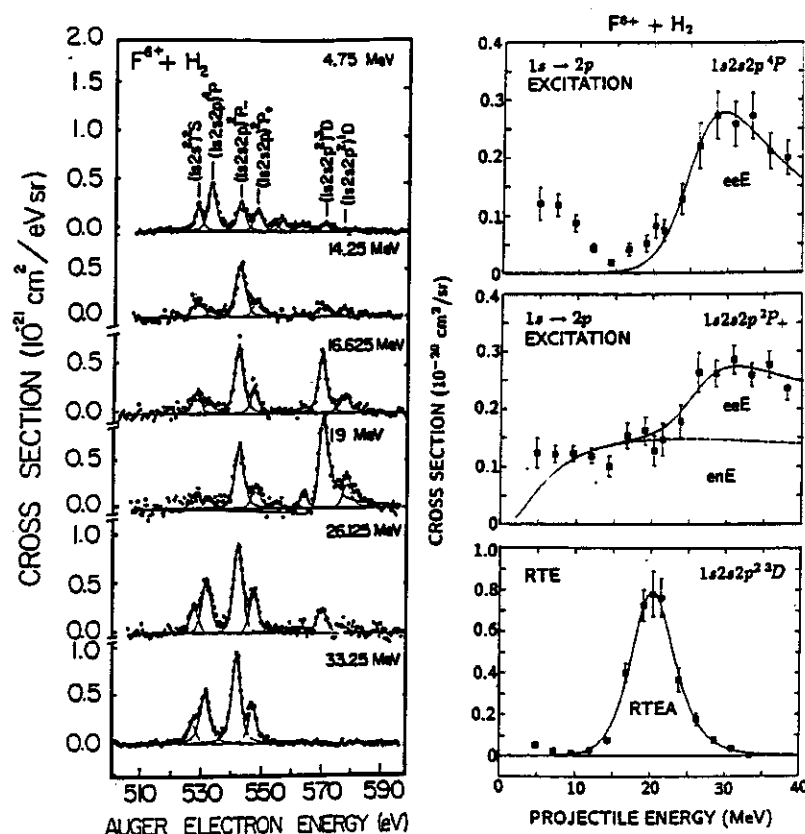


FIGURE 13.25 0° measurements of RTE and e-e Excitation in 5-33 MeV $F^{6+} + H_2$ collisions. Left: High resolution DDCS. Line assignment indicates the first four lines correspond to Li-like lines resulting from $1s \rightarrow 2s, 2p$ excitation. The higher energy lines correspond to Be-like lines formed by TE. Note the resonance behavior of the 3D and 1D lines as the collision energy is varied across the resonance energy at ~ 20 MeV clearly identifying these lines to be produced by RTE. Also notice the behavior of the 4P line which is first seen to decrease with collision energy and then after ~ 19 MeV to start increasing again. This behavior indicates the onset of electron-electron Excitation, once the threshold for eeE is crossed. The projectile energy dependence of the single differential cross sections for the 4P , $^2P_+$ and 3D states (areas under the peaks) are plotted on the right. The $^2P_+$ state is formed by contributions from both enE and eeE. The 4P can only be formed by eeE with spin exchange and by Transfer-Loss below threshold. Direct $1s \rightarrow 2p$ excitation is forbidden due to spin conservation. Furthermore, eeE contributions are zero below the excitation threshold. The 3D state shows the characteristic resonance structure of RTE. Continuous lines are IA calculations, while the chain line is a Born calculation for the enE contribution (adapted from Ref. [73]).

electron-electron Excitation (eeE) and Ionization (eeI)

In the case of electron impact excitation or ionization of ions, there are no resonances as in DC to signal the onset of the e-e interaction. However, in both cases the electron must have enough energy to excite or ionize the ion. Thus, a threshold exists below which the cross section for electron impact is zero. This threshold should also be reflected in the ion-atom counterpart of these electron impact processes (see Table 13.4). In Fig. 13.25 (left) apart from the RTE lines already discussed the rest of the Auger lines are due to Li-like configurations, which are produced by $1s \rightarrow 2\ell$ ($\ell = 0, 1$) excitation. In Fig. 13.25 (right) the differential cross sections measured at $\theta = 0^\circ$ for $1s2s2p^2P_+$ and $1s2s2p^4P$ Auger production and their energy dependence are shown. $\Delta E_{1s \rightarrow 2p} \sim 723$ eV for F^{6+} , which is seen to correspond to a mean collision energy of about 25 MeV. While this would be a sharp threshold for electron impact excitation, in the case of e-e Excitation it is seen that the ion-atom threshold is smeared-out due to the much broader collision energy distribution of the target electron "beam".

It is interesting to note that in the example shown in Fig. 13.25, involving the production of the 4P state in the excitation process $F^{6+}(1s^22s)^2S + H_2 \rightarrow F^{6+}(1s2s2p)^4P$, neither a direct e-e nor e-n excitation can give rise to the 4P state since this would involve a spin flip of the projectile electron. It is well known that a pure Coulomb interaction cannot change the spin of the electron. However, if the active target and projectile electrons are *exchanged* it is possible to obtain a projectile 4P state from an initial 2S state. It is seen in Fig. 13.25(right top) that only e-e contributions are needed for agreement with the data above threshold, indicating the absence of e-n contributions, as expected. In the case of the production of the $(1s2s2p)^2P_+$ state both e-e and e-n can contribute and are thus added incoherently as indicated. It is reminded that the 4P state is metastable and therefore the effective solid angle corrections due to the long lifetime, already discussed in section 13.4.2, must be properly applied to obtain the differential cross section shown in Fig. 13.25.

The case of e-e Ionization is shown in the energy dependence of K-shell ionization cross sections in Fig. 13.26. In the case of $1s$ ionization of C^{2+} the threshold for electron impact ionization is 340 eV which translates into a mean collision energy of ~ 7.5 MeV. For ionization, no sudden change in the energy dependence of the cross section is observed as is seen for e-e Excitation. The reason for this is simple: electron impact excitation involves discrete states and therefore has a very well defined excitation energy ΔE with a sharp threshold. Electron impact ionization involving transitions to a continuum of final states does not have a well defined excitation energy, thus leading to a broadened threshold [8,115].

We finally note that many new significant measurements of e-e Ionization have recently appeared, using techniques other than electron spectroscopy. These use mostly coincidence techniques between recoil target and scattered

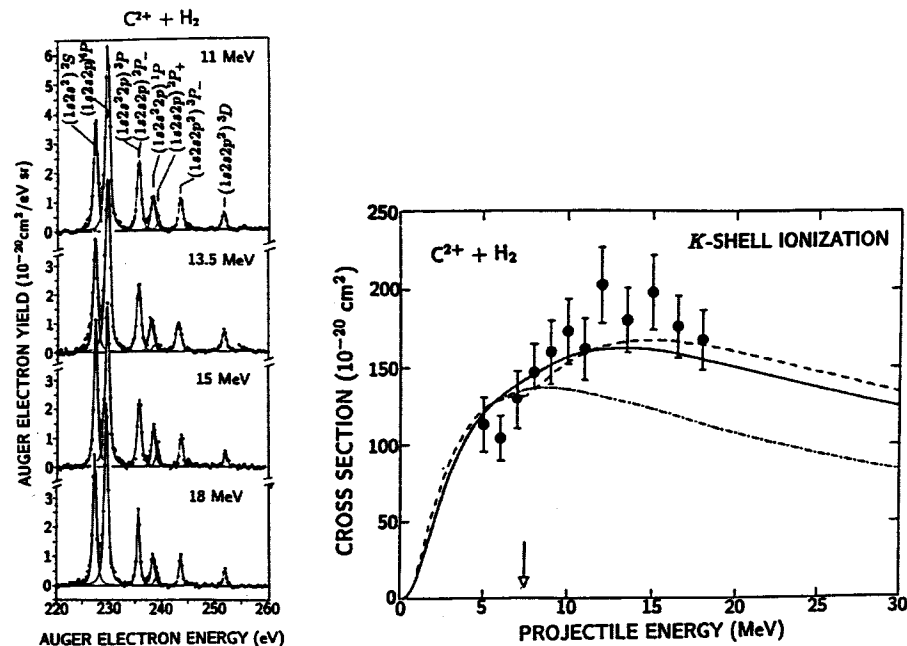


FIGURE 13.26 0° measurement of K-shell projectile ionization in 5-18 MeV C²⁺+H₂ collisions. Left: High resolution normalized electron yields after subtraction of background continuum electrons and transformation to the projectile frame. Line assignment is similar to the case of O⁴⁺ shown in Fig. 13.19. The 1s2s²³S line results from 1s ionization of the ground state. The ⁴P, ²P₋ and ²P₊ states result from 1s ionization of the metastable 1s2s2p³P ion. All other lines are due to the decay of Be-like configurations produced by excitation. Right: Measured K-shell projectile ionization cross section, σ_K . Continuous line: PWBA-IA calculation of $\sigma_K = \sigma_{enI} + \sigma_{eeI}$. Dashed line: PWBA screening-antiscreening calculations of σ_K . Dash-Dotted line: PWBA calculation of σ_K considering only e - n interaction. Arrow indicates projectile energy corresponding to the 1s ionization threshold for electron impact of the same velocity (adapted from Ref. [8]).

projectiles to reduce or isolate the contribution of competing e-n interactions [129,131,9,141,132].

13.6.3 Shape resonances of negative ions

The collisional detachment of an electron from a negative ion is a fundamental process in atomic physics. This process is particularly interesting when it

involves a *resonance*; a transiently-formed state that decays via autodetachment [142]. This resonance lies energetically above its parent state such as the ground state of Li or the excited state of He(1s2p³P), as shown in the inserts of Fig. 13.27. Shape resonances have been studied in low energy electron-atom scattering [143-145] and, to a lesser extent, by photodetachment [146,147]. Recent observations of shape resonances in negative ion collisions with gas targets include the H⁻(2s2p¹P^o) [53-55], the He⁻(1s2p²⁴P) [56], and the Li⁻(2s2p³P) and tentatively the B⁻(2p²¹D) states [57].

Fig. 13.27 shows electron energy spectra obtained with ZAPS in collisions of 100 keV Li⁻ and He⁻ ions with a He gas target. A single-stage spherical-sector spectrometer with mean radius of 35 mm and external pre-retardation was used to achieve high resolution. A channeltron was used to detect the electrons. The spectrometer had an acceptance angle $\Delta\theta \sim 2^\circ - 6^\circ$ depending on where the electrons were detached in the target gas cell. The cell had a length of 37 mm and was placed about 40 mm from the spectrometer entrance slit, which was 2 mm in diameter. Typical measured negative ion currents were 100 pA. Also shown in the inserts are partial energy level diagrams for the Li/Li⁻ and He/He⁻ systems. A signature of the Li⁻ shape resonance is exhibited on both sides of the Cusp peak due to kinematic line doubling (see discussion in section 13.2.1) and the resonance state is identified as the 2s2p³P^o state. It is noted that excitation of this resonant state from the ground state of Li⁻ requires the occurrence of an electron *spin exchange* in the collision [148,143], as in the case of the e-e Excitation of the 1s2s2p⁴P state discussed earlier. In the case of He⁻ the resonance structure dominates and the Cusp peak is not distinguishable, apparently due to a large shape resonance cross section and a very small ratio of resonance energy to the Cusp energy t . Shown in the figures as solid curves are least-square fits to the data points, which are essentially the predicted electron energy spectra. From the fits the energy and width of the resonance state are extracted.

The DDCS consist of contributions arising from the direct (non-resonant) and resonant detachment processes: [53,56,57]

$$\frac{d^2\sigma}{d\epsilon'd\Omega'} = \left(\frac{d^2\sigma}{d\epsilon'd\Omega'} \right)^{NR} + \frac{\alpha\epsilon' + \beta}{1 + \epsilon'^2}, \quad (13.33)$$

where $(d^2\sigma/d\epsilon'd\Omega')^{NR}$ is the direct (non-resonant) contribution which can be parameterized by using $\Sigma_l \Sigma_n a_{ln}(\epsilon') P_l(\cos\theta')$ with a_{ln} being expressed in powers of ϵ' and P_l being Legendre polynomials with l being the angular momentum of the outgoing electron. The reduced energy variable is defined as $\epsilon' = 2(\epsilon' - \epsilon'_r)/\Gamma'$, where the primes refer to projectile frame parameters as used consistently through out this article. In principle, the resonant and non-resonant detachment channels may interfere. This possibility is included by using the Shore (or Fano) parameters α and β . The resonance is characterized in the usual manner by an energy ϵ'_r and a width Γ' .

The contribution from the resonances is shown in the bottom curves in the

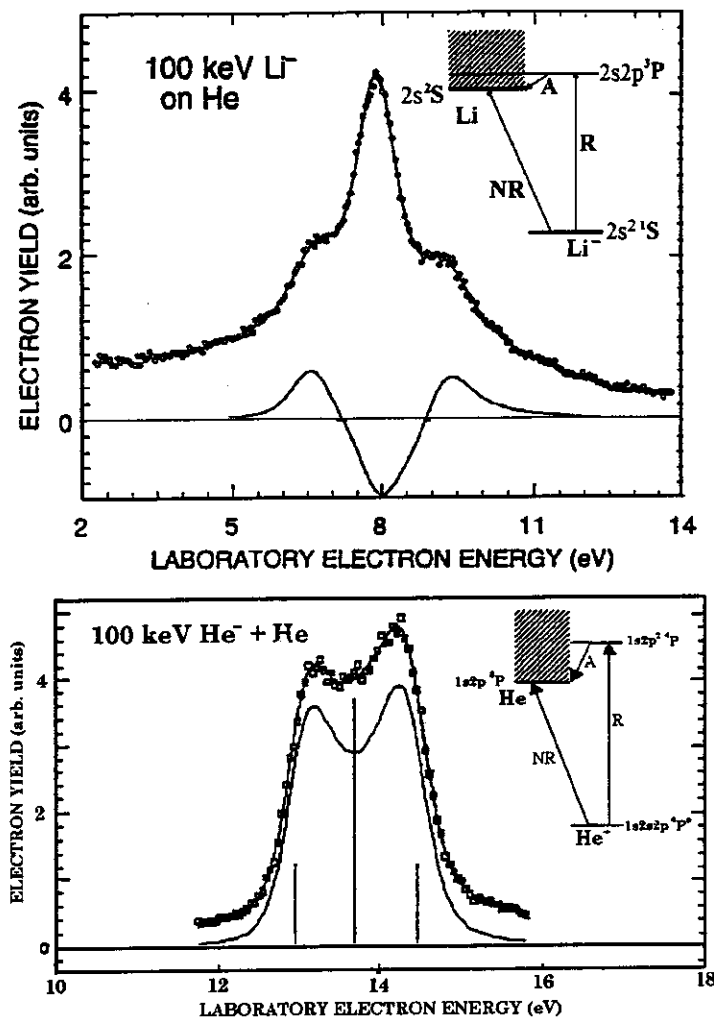


FIGURE 13.27 0° measurement of shape resonances using ZAPS in 100 keV Li^- and $\text{He}^- + \text{He}$ collisions. The spectra indicate the central Cusp peak and the kinematically doubled resonance structures. The solid curve through the data points represent least square fits, while the bottom curves indicate the contribution of the shape resonances including interference. Inserts: Partial energy level diagrams for Li/Li^- and He/He^- systems. Resonant (R) and non-resonant (NR) detachment is shown. The shape resonance decays via autodetachment (A) leaving the residual atom in the ground state, in the case of Li and in the $1s2p^3P$ state for He. The resonance parameters extracted from the fits are for Li, $\epsilon_r' = 50 \pm 6$ meV and $\Gamma' = 64 \pm 25$ meV [57] and for He, $\epsilon_r' = 11$ meV and $\Gamma' = 8$ meV (adapted from Ref. [57]).

figure. It can be seen that there exists appreciable destructive interference, for the case of Li^- detachment, in the region of the cusp corresponding to the threshold region in the ion frame. This could possibly be due to the presence of a virtual state such as the theoretically predicted 3S state [144]. The extracted values of the resonance parameters allow for the identification of the observed structure with the $2s2p^3P$ shape resonance state in Li^- , which until now [57] has defied experimental investigation even though it has been the subject of numerous calculations over the past few decades [143,144,149]. This is primarily due to the experimental difficulty of detecting the very low energy electrons ejected in the autodetaching decay and the fact that the state is not efficiently optically coupled to the 1S ground state of Li^- , thereby prohibiting photodetachment studies. These problems however are overcome using ZAPS since the electron energies are now kinematically shifted into a more experimentally accessible energy region. For example, in the measurements at 100 keV the ratio of the energies of the detached electrons in the laboratory frame to those in the ion frame was more than two orders of magnitude. The measured energy and width of the $\text{He}^-(1s2p^2^4P)$ shape resonance [56] agreed well with the more accurate results obtained by Walter *et al.* [147] who employed photoabsorption to selectively excite this resonance state.

13.7 FUTURE PROSPECTS

Zero-degree Auger projectile spectroscopy can be relied to provide state-selective cross section information about ion-atom collision processes for years to come, particularly for low Z -ions ($Z \leq 10$) where comparable x-ray techniques are much more tedious. Past and present work has focused primarily on singles K-Auger spectra of few electron ions in collisions with H_2 and He targets, conditions which give rise to rather simple and well resolved lines.

Future applications could be extended to heavier projectiles, L-Auger studies and to ions with more than 4 electrons, as well as collisions utilizing heavier, crystalline or laser-excited targets. High resolution measurements in coincidence with the scattered projectile could provide information on the orientation [99,100] of the intermediate formed states and help identify collision processes under non-needle ionization conditions. Measurements of electrons in coincidences with recoils could provide more information about e-e interactions [115], particularly when combined with the technique of recoil ion momentum spectroscopy [150] (see also corresponding chapter in this volume).

In the last few years we have also witnessed the coming of age of ion storage rings and ion traps for use in atomic physics, providing new possibilities for studying both ion-atom and electron-ion collision processes with unprecedented beam energy resolution and intensity. ZAPS has yet to be used in these new collision environments. In particular, applied to the study of cooled ions in storage rings, ZAPS should in principle provide electron spectra of unprecedented quality given the much higher beam intensity and smaller energy

spread of these beams. Applications to the study of ions excited by electron impact are also under way [151].

The viability of these new applications of ZAPS will necessarily require the use of much more efficient electron spectrometers utilizing position sensitive electron detectors [99,100] and possibly double focusing devices. Already such analyzers are under construction and are expected to provide the 2nd generation ZAPS devices.

ACKNOWLEDGMENTS

We are particularly indebted to our colleagues Pat Richard at Kansas State University and Nico Stolterfoht at HMI-Berlin. We would like to thank them for their unmitigated support and guidance through out our extensive collaboration. Much of the reported development of ZAPS was undertaken in the stimulating and well equipped environments of the HMI and Kansas State collision laboratories.

We would also like to thank Geraldo Sigaud of PUC-Rio for his critical reading of the manuscript, Gabor Toth and Martin Grether for communicating unpublished results and Nektarios Sartzetakis for his kind technical support with the electronic conversion of the figures.

T.J.M.Z. would like to acknowledge partial support by the Division of Chemical Sciences, Office of Basic Energy Science, Office of Energy Research, U.S. Department of Energy and NATO collaborative research grant CRG-910567.

REFERENCES

1. R. K. Janev and H. Winter, *Phys. Rev.* **117**, 265 (1985).
2. H. P. Summers and W. J. Dickson, in *Recombination of Atomic Ions*, NATO Advanced Study Institute Series B: Physics, edited by W. G. Graham, W. Fritsch, Y. Hahn, and J. Tanis (Plenum Publishing Corp, New York, 1992), Vol. 296, pp. 31-48.
3. R. L. Becker, A. L. Ford, and J. F. Reading, *Phys. Rev. A* **29**, 311 (1984).
4. N. Stolterfoht, in *Spectroscopy and Collisions of Few-Electron Ions*, edited by M. Ivascu, V. Florescu, and V. Zoran (World Scientific, Singapore, New Jersey, London, 1989), p. 342.
5. N. Stolterfoht, *Phys. Scr.* **42**, 192 (1990).
6. J. H. McGuire, *Adv. At. Mol. & Opt. Phys.* **29**, 217 (1992).
7. T. J. M. Zouros, in *Recombination of Atomic Ions*, NATO Advanced Study Institute Series B: Physics, edited by W. G. Graham, W. Fritsch, Y. Hahn, and J. Tanis (Plenum Publishing Corporation, New York, 1992), Vol. 296, pp. 271-300.
8. D. H. Lee *et al.*, *Phys. Rev. A* **46**, 1374 (1992).
9. E. C. Montenegro, W. E. Meyerhof, and J. H. McGuire, *Adv. At. Mol. & Opt. Phys.* **34**, 249 (1994).

10. T. J. M. Zouros, in *Applications of Particle and Laser Beams in Materials Technology*, NATO Advanced Study Institute Series E: Applied Sciences, edited by P. Misailides (Kluwer Academic Publishers, Netherlands, 1995), Vol. 283, pp. 37-52.
11. T. J. M. Zouros, *Comments At. & Mol. Phys.* **32**, 291 (1996).
12. I. A. Sellin, in *Topics in Current Physics*, edited by S. Bashkin (Springer, Heidelberg, 1976), Vol. 1, p. 265.
13. D. L. Matthews, in *Atomic Physics: Accelerators*, Vol. 17 of *Methods of Experimental Physics*, edited by P. Richard (Academic Press, New York, 1980), pp. 433-527.
14. M. E. Rudd and J. H. Macek, in *Case Studies in Atomic Physics*, edited by E. W. McDaniels and M. C. McDowell (North-Holland, Amsterdam, 1972), Vol. 3, pp. 47-136.
15. N. Stolterfoht *et al.*, *Phys. Rev. A* **12**, 1313 (1975).
16. R. Bruch *et al.*, *Phys. Rev. A* **19**, 587 (1979).
17. M. Rødbør *et al.*, *J. Phys. B* **10**, L483 (1977).
18. M. Rødbør, R. Bruch, and P. Bisgaard, *J. Phys. B* **12**, 2413 (1979).
19. R. Morgenstern, A. Niehaus, and U. Thielmann, *Phys. Rev. Lett.* **37**, 199 (1976).
20. R. Morgenstern, A. Niehaus, and U. Thielmann, *J. Phys. B* **10**, 1039 (1977).
21. R. Morgenstern, A. Niehaus, and G. Zimmermann, *J. Phys. B* **13**, 4811 (1980).
22. A. Itoh *et al.*, *J. Phys. B* **16**, 3965 (1983).
23. A. Itoh *et al.*, *Phys. Rev. A* **31**, 684 (1985).
24. A. Itoh *et al.*, *J. Phys. B* **18**, 4581 (1985).
25. T. J. M. Zouros, D. Schneider, A. Itoh, and N. Stolterfoht, *Phys. Rev. A* **35**, 1963 (1987).
26. T. J. M. Zouros, D. Schneider, and N. Stolterfoht, *Nucl. Instrum. Methods Phys. Res. Sect. B* **31**, 349 (1988).
27. N. Stolterfoht, *Phys. Rep.* **146**, 315 (1987).
28. N. Stolterfoht, *J. Electr. Spectr. and Rel. Phenom.* **67**, 309 (1994).
29. M. L. A. Raphaelian, H. G. Berry, and N. B. Mansour, *Phys. Rev. A* **43**, 4071 (1991).
30. N. Stolterfoht *et al.*, *Phys. Rev. Lett.* **57**, 74 (1987).
31. R. Mann and H. Schulte, *Z. Phys. D* **4**, 343 (1987).
32. R. Mann, *Phys. Rev. A* **35**, 4988 (1987).
33. H. A. Sakaue *et al.*, *J. Phys. B* **23**, L401 (1990).
34. H. A. Sakaue *et al.*, *J. Phys. B* **24**, 3787 (1991).
35. J. K. Swenson *et al.*, *Phys. Rev. Lett.* **57**, 3042 (1986).
36. T. J. M. Zouros, D. Schneider, and N. Stolterfoht, *J. Phys. B* **21**, L671 (1988).
37. T. J. M. Zouros *et al.*, *Phys. Rev. A* **40**, 6246 (1989).
38. T. J. M. Zouros, C. P. Bhalla, D. H. Lee, and P. Richard, *Phys. Rev. A* **42**, 678 (1990).
39. D. H. Lee *et al.*, *Phys. Rev. A* **44**, 1636 (1991).
40. T. J. M. Zouros, D. H. Lee, and P. Richard, *Phys. Rev. Lett.* **62**, 2261 (1989).
41. S. Ricz, B. Sulik, N. Stolterfoht, and I. Kádár, *Phys. Rev. A* **47**, 1930 (1993).

42. B. Sulik *et al.*, Phys. Rev. A **52**, 387 (1995).
43. T. J. M. Zouros, D. H. Lee, P. Richard, and J. M. Sanders, Nucl. Instrum. Methods Phys. Res. Sect. B **56/57**, 107 (1991).
44. R. Bruch *et al.*, Phys. Rev. A **35**, 4114 (1987).
45. P. Focke *et al.*, Phys. Rev. A **40**, 5633 (1989).
46. I. Kádár *et al.*, Phys. Rev. A **44**, 2900 (1991).
47. M. Sataka *et al.*, Phys. Rev. A **44**, 7290 (1991).
48. D. Schneider *et al.*, Phys. Rev. A **34**, 169 (1986).
49. W. D. Zeitz, R. Kowallik, and D. Schneider, Phys. Rev. A **39**, 43 (1989).
50. B. D. DePaola *et al.*, J. Phys. B **29**, 1247 (1996).
51. C. Liao *et al.*, Nucl. Instrum. Methods Phys. Res. Sect. B **98**, 324 (1995).
52. T. J. M. Zouros *et al.*, Nucl. Instrum. Methods Phys. Res. Sect. B **99**, 27 (1995).
53. L. H. Andersen, J. P. Bangsgaard, and J. Sørensen, Phys. Rev. Lett. **57**, 1558 (1986).
54. M. M. Duncan and M. G. Menendez, Phys. Rev. A **39**, 1534 (1989).
55. F. Penent, J. P. Grouard, J. L. Montmagnon, and R. I. Hall, J. Phys. B **25**, 2831 (1992).
56. P. A. Zavodsky, L. Sarkadi, L. Víkor, and J. Pálinkás, Phys. Rev. A **50**, 899 (1994).
57. D. H. Lee, W. D. Brandon, D. Hastorp, and D. J. Pegg, Phys. Rev. A **53**, R633 (1996).
58. Y. Yamazaki *et al.*, Phys. Rev. Lett. **57**, 992 (1986).
59. Y. Yamazaki *et al.*, Phys. Rev. Lett. **61**, 2913 (1988).
60. J. K. Swenson *et al.*, Phys. Rev. Lett. **63**, 35 (1989).
61. J. K. Swenson *et al.*, Phys. Rev. Lett. **66**, 417 (1991).
62. D. H. Lee *et al.*, Nucl. Instrum. Methods Phys. Res. Sect. B **56/57**, 99 (1991).
63. N. Stolterfoht *et al.*, Nucl. Instrum. Methods Phys. Res. Sect. B **24/25**, 168 (1987).
64. T. J. M. Zouros *et al.*, Nucl. Instrum. Methods Phys. Res. Sect. B **40/41**, 17 (1989).
65. P. Richard, in *X-Ray and Inner-Shell Processes*, edited by T. A. Carlson, M. O. Krause, and S. T. Manson (AIP, New York, 1990), p. 315.
66. B. D. DePaola, Nucl. Instrum. Methods Phys. Res. Sect. B **56/57**, 154 (1991).
67. N. Stolterfoht, Phys. Scr. **T51**, 39 (1994).
68. N. Stolterfoht, in *Two-Center Effects In Ion-Atom Collisions*, edited by T. J. Gay and A. F. Starace (American Institute of Physics Conference Series, New York, 1996), Vol. 362, p. 163.
69. Y. S. Gordeev and G. N. Ogurtsov, Sov. Phys. JETP **33**, 1105 (1971).
70. J. R. Risley, A. K. Edwards, and R. Geballe, Phys. Rev. A **9**, 1115 (1974).
71. A. Gleizes, P. Benoit-Cattin, A. Bordenave-Montesquieu, and A. Merchez, J. Phys. B **9**, 476 (1976).
72. P. Dahl, M. Rødbør, B. Fastrup, and M. E. Rudd, J. Phys. B **9**, 1567 (1976).
73. D. H. Lee, Ph.D. dissertation, Kansas State University, 1990, (unpublished).
74. T. J. M. Zouros and M. Wilson, in *Europhysics Conference Abstracts*, edited by R. C. Thompson (European Physical Society, Edinburgh, UK, 1995), Vol. 19A, p. 67.
75. D. Schneider *et al.*, Nucl. Instrum. Methods Phys. Res. Sect. B **24/25**, 173 (1987).
76. D. H. Lee *et al.*, Nucl. Instrum. Methods Phys. Res. Sect. B **40/41**, 1229 (1989).
77. B. D. DePaola *et al.*, Nucl. Instrum. Methods Phys. Res. Sect. B **40/41**, 187 (1989).
78. P. G. Burke and D. D. McVicar, Proc. Phys. Soc. **86**, 989 (1965).
79. D. Schneider, C. F. Moore, and B. M. Johnson, J. Phys. B **9**, L153 (1976).
80. N. Stolterfoht, H. Gabler, and U. Leithäuser, Phys. Rev. Lett. **45**, 351 (1973).
81. N. Stolterfoht, D. Schneider, R. Mann, and F. Folkmann, J. Phys. B **10**, L281 (1977).
82. H. Tawara, P. Richard, K. A. Jamison, and T. J. Gray, J. Phys. B **11**, L615 (1978).
83. H. Tawara *et al.*, Phys. Rev. A **20**, 2340 (1979).
84. H. Tawara *et al.*, Phys. Rev. A **19**, 1960 (1979).
85. M. Terasawa *et al.*, Phys. Rev. A **27**, 2868 (1983).
86. M. Zhu *et al.*, Nucl. Instrum. Methods Phys. Res. Sect. B **98**, 351 (1995).
87. K. D. Sevier, *Low Energy Electron Spectrometry* (Wiley, New York, 1972).
88. D. W. O. Heddle, *Electrostatic Lens Systems* (Adam Hilger, Bristol, 1991).
89. M. Grether, Ph.D. dissertation, TU-Berlin, 1995.
90. J. H. Moore, C. C. Davis, and M. A. Coplan, *Building Scientific Apparatus* (Addison-Wesley, London, 1983).
91. G. A. Harrower, Rev. Sci. Instrum. **26**, 850 (1955).
92. V. P. Afanas'ev and S. Y. Yavor, Sov. Phys. Tech. Phys. **20**, 715 (1976), [Translation of Zh. Tekh. Fiz. **45**, 1137-70 (1975)].
93. W. Steckelmacher and M. W. Lucas, J. Phys. E **12**, 961 (1979).
94. P. Allard and J.-D. Carette, Can. J. Phys. **49**, 2132 (1971).
95. Y. Delage and J.-D. Carette, Can. J. Phys. **49**, 2118 (1971).
96. D. Roy and J.-D. Carette, Can. J. Phys. **49**, 2138 (1971).
97. N. Stolterfoht, in *Fundamental Processes in Energetic Atomic Collisions*, edited by H. O. Lutz, J. S. Briggs, and H. Kleinpoppen (Plenum, New York, 1983), Vol. 103, pp. 295-318.
98. M. Mack *et al.*, Phys. Rev. A **39**, 3846 (1989).
99. H. Khemliche, M. H. Prior, and D. Schneider, Phys. Rev. Lett. **74**, 5013 (1995).
100. M. H. Prior and H. Khemliche, in *XIX International Conference on the Physics of Electronic and Atomic Collisions (Abstracts 19th ICPEAC)*, edited by L. J. Dubé, J. B. A. Mitchell, J. W. McConkey, and C. E. Brion (American Institute of Physics Conference Series, Woodbury, NY, 1995), Vol. 360, p. 557.
101. F. Bordoni, Nucl. Instrum. & Methods **97**, 405 (1971).
102. D. H. Lee *et al.*, Phys. Rev. A **41**, 4816 (1990).
103. B. Sulik and N. Stolterfoht, in *Accelerator-based atomic physics techniques and applications*, edited by S. M. Shafroth and J. C. Austin (American Institute

- of Physics Conference Series, New York, 1996).
104. N. Stolterfoht *et al.*, Phys. Rev. Lett. **33**, 59 (1974).
 105. J. S. Lee, J. Chem. Phys. **66**, 4906 (1977).
 106. P. D. Fainstein, V. H. Ponce, and R. D. Rivarola, J. Phys. B **22**, 1207 (1989).
 107. L. Gulyás, P. D. Fainstein, and A. Salin, J. Phys. B **28**, 245 (1995).
 108. P. Richard *et al.*, J. Phys. B **23**, L213 (1990).
 109. C. P. Bhalla and R. Shingal, J. Phys. B **24**, 3187 (1991).
 110. D. R. Schultz and R. E. Olson, J. Phys. B **24**, 3409 (1991).
 111. R. L. Arnoldy, P. O. Isaacson, D. F. Gats, and L. W. Choy, Rev. Sci. Instrum. **44**, 172 (1973).
 112. C. W. Woods *et al.*, Phys. Rev. A **13**, 1358 (1976).
 113. T. J. M. Zouros *et al.*, in *DAMOP*, edited by APS (APS, New York, 1994).
 114. T. J. M. Zouros *et al.*, Phys. Rev. A **49**, 3155 (1994).
 115. T. J. M. Zouros *et al.*, Phys. Rev. A **53**, 2272 (1996).
 116. T. Brage and C. F. Fisher, Phys. Rev. A **44**, 72 (1991).
 117. T. Andersen *et al.*, Phys. Rev. A **47**, 890 (1993).
 118. M. H. Chen, B. Crasemann, and H. Mark, Phys. Rev. A **27**, 544 (1983).
 119. S. Schumann, K. O. Groenveld, G. Nolte, and B. Fricke, Z. Phys. A **289**, 245 (1979).
 120. We note that correction factor G_r is equivalent to factor $\frac{1}{G_n}$ introduced in Ref. [8].
 121. R. Mann, S. Hagmann, and L. Weitzel, Nucl. Instrum. Methods Phys. Res. Sect. B **34**, 403 (1988).
 122. H. I. Hidmi, P. Richard, and I. Ben-Itzhak, Nucl. Instrum. Methods Phys. Res. Sect. B **88**, 313 (1994).
 123. W. Mehlhorn, Electron spectrometry of Auger and autoionizing states: Experiment and Theory, Univ. of Aarhus summer lecture notes (unpublished) (1978).
 124. N. Stolterfoht, D. Schneider, and P. Ziem, Phys. Rev. A **10**, 81 (1974).
 125. M. O. Krause *et al.*, Phys. Lett. **31A**, 81 (1970).
 126. J. J. Mackey *et al.*, J. Phys. B **7**, L447 (1974).
 127. A. Jain, C. D. Lin, and W. Fritsch, Phys. Rev. A **39**, 1741 (1989).
 128. J. A. Tanis, in *Recombination of Atomic Ions*, NATO Advanced Study Institute Series B: Physics, edited by W. G. Graham, W. Fritsch, Y. Hahn, and J. Tanis (Plenum Publishing Corp, New York, 1992), Vol. 296, pp. 241-257.
 129. H. P. Hülskötter, W. E. Meyerhof, E. Dillard, and N. Guardala, Phys. Rev. Lett. **63**, 1938 (1990).
 130. M. B. Shah and H. B. Gilbody, J. Phys. B **24**, 977 (1991).
 131. E. C. Montenegro, W. S. Melo, W. E. Meyerhof, and A. G. de Pinho, Phys. Rev. Lett. **69**, 3033 (1992).
 132. W. Wu *et al.*, Phys. Rev. Lett. **72**, 3170 (1994).
 133. R. Moshhammer *et al.*, Phys. Rev. Lett. **73**, 3371 (1994).
 134. R. Gayet, J. Hanssen, A. Martinez, and R. Rivarola, Comments At. & Mol. Phys. **30**, 231 (1994).
 135. R. Gayet, J. Hanssen, and L. Jacqui, J. Phys. B **28**, 2193 (1995).
 136. J. A. Tanis *et al.*, Phys. Rev. Lett. **49**, 1325 (1982).
 137. J. A. Tanis *et al.*, Phys. Rev. Lett. **53**, 2551 (1984).
 138. D. H. Lee *et al.*, in *12th Int. Conf. on Atomic Physics: Abstracts of Contributed Papers*, edited by W. Baylis, G. W. F. Drake, and J. W. McConkey (Univ. of Michigan, Ann Arbor, MI, 1990).
 139. R. C. Parameswaran, C. P. Bhalla, B. P. Walch, and B. D. DePaola, Phys. Rev. A **43**, 5929 (1991).
 140. R. Parameswaran *et al.*, Phys. Rev. A **47**, 3801 (1993).
 141. R. Dörner *et al.*, Phys. Rev. Lett. **72**, 3166 (1994).
 142. H. S. W. Massey, *Negative Ions* (Cambridge Univ. Press, New York, 1976).
 143. D. W. Norcross, J. Phys. B **4**, 1458 (1971).
 144. A.-L. Sinfailam and R. K. Nesbet, Phys. Rev. A **7**, 1987 (1973).
 145. J. Yuan and Z. Zhang, J. Phys. B **22**, 2751 (1989).
 146. H. C. Bryant *et al.*, Phys. Rev. Lett. **38**, 228 (1977).
 147. C. W. Walter, J. A. Seifert, and J. R. Peterson, Phys. Rev. A **50**, 2257 (1994).
 148. N. F. Mott and H. S. W. Massey, *The Theory of Atomic Collisions* (Oxford University Press, London, 1965).
 149. I. I. Fabrikant, Opt. Spectros. (USSR) **53(2)**, 131 (1982).
 150. J. Ullrich *et al.*, Comments At. & Mol. Phys. **30**, 285 (1994).
 151. A. Frank, A. Müller, A. Liedtke, and H. Schnell, Annual report, Institut für Strahlenphysik Universität Stuttgart (1995).